Geophysical Research Letters

RESEARCH LETTER
10.1029/2025GL121543

Key Points:
- A M_w 4.2 earthquake in central Alaska was preceded by 43 s of seismic signals, including a M_w 3.8 very-low-frequency earthquake
- The event occurred at 18 km depth within an intraplate strike-slip fault zone
- The observations motivate future work to understand the conditions leading to earthquake nucleation and rupture

Supporting Information:

Supporting Information may be found in the online version of this article.

Correspondence to:

A. M. McPherson,
ammcpherson.alaska@gmail.com

Citation:

McPherson, A. M., Tape, C., & Kaneko, Y. (2026). Observational evidence of a very-low-frequency earthquake (M_w 3.8) leading to an earthquake (M_w 4.2): Minto Flats strike-slip fault zone, central Alaska. *Geophysical Research Letters*, *53*, e2025GL121543. https://doi.org/10.1029/2025GL121543

Received 8 JAN 2026
Accepted 20 MAY 2026

Observational Evidence of a Very-Low-Frequency Earthquake (M_w 3.8) Leading to an Earthquake (M_w 4.2): Minto Flats Strike-Slip Fault Zone, Central Alaska

A. M. McPherson[1], **C. Tape**[1], **and Y. Kaneko**[2]

[1]University of Alaska Fairbanks, Fairbanks, AK, USA, [2]Kyoto University, Kyoto, Japan

Abstract The physical conditions governing earthquake initiation are largely unknown, particularly in the minutes to seconds preceding rupture. While there is geodetic and seismic evidence of precursory activity in the hours to weeks prior to large earthquakes, the observational evidence immediately preceding the earthquake rupture is limited and controversial. Here we present evidence of a well-recorded earthquake from the Minto Flats fault zone in central Alaska having 43 s of high-frequency precursory signals. Within these signals was a M_w 3.8 very-low-frequency earthquake (VLFE) on a dipping strike-slip fault. The VLFE was followed by a M_w 4.2 earthquake having the same focal mechanism as the VLFE. The distinct signals and the close similarity in focal mechanisms between the VLFE and the earthquake provide evidence for a slow-to-fast rupture transition during earthquake initiation.

Plain Language Summary Earthquakes tend to start without warning and under conditions that are not understood. There are few reliable observations of seismic activity immediately prior to an earthquake rupture. In August of 2025 in central Alaska, a M_w 4.2 earthquake occurred and was preceded by 43 s of an unusual signal containing high-frequency bursts as well as a M_w 3.8 low-frequency event. These well-recorded observations demonstrate connectivity among three types of earthquakes to form a single, larger and longer event. The observations may be useful for other efforts in laboratory experiments and computer modeling to understand how earthquakes begin and how they grow.

1. Introduction

The questions of how and when earthquakes begin constitute an elusive quest of seismology. This quest encompasses efforts within laboratory experiments, numerical modeling, and observational studies of seismic and geodetic data. Laboratory studies demonstrate that microearthquakes can nucleate with observable precursory behavior (Latour et al., 2013; McClaskey, 2019; Ohnaka & Shen, 1999; Yamashita et al., 2021), while numerical models based on rate-and-state friction provide theoretical frameworks for nucleation and fault frictional instability (Cattania & Segall, 2021; Dieterich, 1992; R. Ito & Kaneko, 2023; Kaneko et al., 2016; Rubin & Ampuero, 2005; Yabe & Ide, 2018). Observationally, geodetic measurements have revealed aseismic slip preceding some large earthquakes, including the 2011 M_w 9.1 Tohoku and 2014 M_w 8.1 Iquique events (Y. Ito et al., 2013; Kato et al., 2012; Ruiz et al., 2014; Schurr et al., 2014). These observations suggest that slow deformation may play a role in earthquake initiation, although the extent and generality of such processes remain debated.

On time scales of seconds to minutes prior to the onset of earthquakes, observational evidence has been controversial. For example, a nucleation phase identified in earlier studies (Beroza & Ellsworth, 1996; Ellsworth & Beroza, 1995; Iio, 1995) was explained in terms of anelastic attenuation by Mori and Kanamori (1996). Foreshock signals from the 1999 Izmit earthquake were interpreted as aseismic slip (Bouchon et al., 2011) and then later identified as a normal foreshock sequence (Ellsworth & Bulut, 2018). Recent syntheses emphasize that multiple physical processes may contribute to earthquake nucleation, including aseismic slip, stress transfer, and rock damage, with their relative importance varying across tectonic settings (Gomberg, 2018; Kato & Ben-Zion, 2021; Martínez-Garzón & Poli, 2024; Peng & Lei, 2025). Observations that can clearly resolve the temporal and spatial evolution of earthquake nucleation therefore remain rare and valuable.

The Minto Flats fault zone (MFFZ) in central Alaska (Figure 1) is a left-lateral intraplate strike-slip fault zone that records hundreds of microearthquakes and a few M_w 3–4 earthquakes each year (Page et al., 1995; Sims

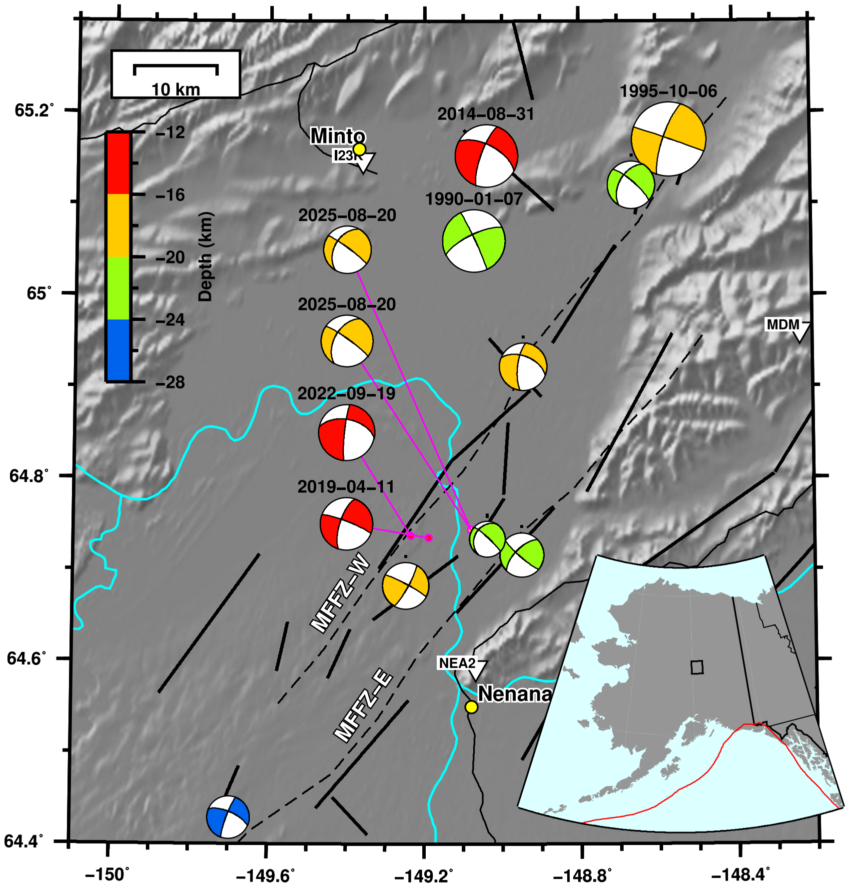

Figure 1. Minto Flats fault zone (MFFZ), central Alaska, with source mechanisms of notable events, including four featured in this study: the VLFE and earthquake on 2025-08-20 (2 yellow beachballs directly under Minto and I23K), an earthquake on 2019-04-11 (Smith et al., 2023), and an earthquake on 2022-09-19. Other events include the six featured in Tape et al. (2018) and three larger events: 1995-10-05 M_w 6.0, 2014-08-31 M_w 5.0, and 1990-01-07 M_L5.0. MFFZ is depicted by the two dashed black lines (MFFZ-W, MFFZ-E); a more detailed representation of the fault zone is represented by the black segments, which are digitized from relocated seismicity (Sims et al., 2026). Among the 41 stations used in this study, three are within this region: NEA2 (Nenana), I23K (Minto), and MDM (Murphy Dome). The inset map of Alaska depicts the expanded region as the black box, as well as the plate boundary (red) between Pacific and North America.

et al., 2026; Tape et al., 2015). A small portion of these events have produced intriguing observations of precursory signals, including a M_w 3.8 earthquake in 2012 that was preceded by a 24 s high-frequency foreshock triggered by distant surface waves (Tape et al., 2013), and a M_w 3.8 very-low-frequency earthquake (VLFE) in 2015 characterized by long-duration, low-frequency energy (Tape et al., 2018). A subsequent M_w 3.7 earthquake in 2016 exhibited both high-frequency and low-frequency signals without remote triggering, suggesting that VLFEs may play a recurring role in earthquake initiation within the MFFZ.

In August 2025, a M_w 4.2 earthquake occurred in MFFZ and was immediately preceded by a well-recorded M_w 3.8 VLFE, which in turn was preceded by a high-frequency signal. This three-part event provides a rare opportunity to examine the temporal and spatial relationship between a VLFE and a subsequent earthquake. Here we analyze low-frequency and high-frequency seismic observations to constrain the source properties of both events and to characterize their temporal evolution.

2. Methods and Results

We analyze the events in MFFZ by estimating moment tensors and by carefully examining waveforms filtered with different pass bands. We retrieve three-component seismic recordings for broadband stations within 300 km of the epicenters. We extract 400 s time series (100 s before the origin time, 300 s after), we remove the instrument response, and we convert the recordings to displacement.

Table 1
Source Parameters of Events in This Study

Event	Origin time (UTC)	s	Longitude (°)	Latitude (°)	Depth (km)	Magnitude
2015 earthquake	2015-10-22 13:16:15.8 [C]	–	−149.0388 [C]	64.7334 [C]	21 [T]	M_w 2.85 [T]
2019 earthquake	2019-04-11 10:42:45.5 [C]	–	−149.1890 [C]	64.7350 [C]	14 [T]	M_w 4.20 [T]
2022 earthquake	2022-09-19 01:15:28.8 [C]	–	−149.2350 [C]	64.7370 [C]	15 [T]	M_w 4.50 [T]
2025 earthquake	2025-08-20 20:35:27.7 [C]	0	−149.0810 [C]	64.7440 [C]	18 [T]	M_w 4.15 [T]
2025 VLFE	2025-08-20 20:35:04.1 [T]	−23.6	−149.0810 [T]	64.7440 [T]	18 [T]	M_w 3.80 [T]
2025 HFF signal	2025-08-20 20:34:45.2 [C]	−42.5	−149.0890 [C]	64.7240 [C]	16.0 [C]	M_L 3.0 [C]

Note. The letters denote the source of values: C = AEC catalog, T = this study. The third column is the origin time relative to the 2025 earthquake origin time. The AEC catalog depth and magnitude for the 2025 earthquake are 15.4 km and M_L 4.2. Estimated source mechanisms are listed in Table S1. VLFE = very-low-frequency earthquake; HFF = high-frequency foreshock.

In addition to the three-part 2025 M_w 4.2 event, we examine two comparison earthquakes in the fault zone: 2019 M_w 4.2 and 2022 M_w 4.5. We estimate double-couple moment tensors by fitting P waves and surface waves from all three components. The moment tensor is parameterized by four parameters: magnitude (M_w) and three angles (strike, dip, rake) defining the orientation. For each magnitude and mechanism, we calculate synthetic seismograms using a standard 1D Earth model for the region (tactmod: Beaudoin et al., 1992; Ratchkovski & Hansen, 2002), and we quantify the waveform misfit between synthetic seismograms and observed seismograms. The estimated moment tensor is the one that provides the minimum misfit. This grid search is implemented in the software MTUQ (Thurin et al., 2025), which builds upon previous efforts (Silwal & Tape, 2016; Zhao & Helmberger, 1994; Zhu & Helmberger, 1996).

Table 1 lists a combination of source parameters determined by the Alaska Earthquake Center (AEC) and by this study. AEC analysts picked P waves for the 2025 earthquake, as well as P waves for an emergent high-frequency foreshock (HFF) signal that started about 40 s earlier (Figure S1 in Supporting Information S1). The catalog hypocenter of the earthquake differs from that of the HFF signal by 2.3 km (2.2 km horizontally and 0.6 km vertically). Given the uncertainty in the HFF onset times (Section 2.2), we assume the uncertainties in the HFF hypocenter are a few km.

A low-frequency waveform—characterizing the VLFE—occurs concurrently with the 2025 HFF signal, beginning approximately 20 s after the onset of the HFF signal. The VLFE waveforms were not analyzed by AEC analysts and therefore there is no catalog hypocenter or origin time. For modeling purposes, we choose to assign the VLFE hypocenter to the earthquake hypocenter (Table 1), and later we discuss the location of the VLFE relative to the earthquake.

2.1. Low-Frequency Analysis of the 2025 Events

Figure 1 displays moment tensors from previous studies and from the four events featured in this study. These events are well-covered by the regional network (e.g., Figure S2 in Supporting Information S1), enabling robust estimation of source mechanisms. The stability of the mechanisms is also reflected in the grid searches over depth (Figure S3 in Supporting Information S1).

The first moment tensor we estimated was for the 2025 earthquake; the surface wave fits (bandpass 16–30 s) are exceptionally good, as shown by the 13 closest stations in Figure 2b. The P waveforms (bandpass 1.5–4.0 s) also appear to fit well, though there are clearly unfit observed waveforms prior to the synthetic P wave (e.g., NEA2 at 17 km epicentral distance); these waves turn out not to be noise but are associated with a preceding event. To demonstrate the reliability of the recorded P waves and the stability of the estimated moment tensor, we perform a P-wave only inversion (McPherson, 2025).

The low-frequency waveforms for the 2025 event revealed lower-amplitude signals starting about 20–25 s prior to the main (surface wave) earthquake arrival. These signals—unassociated with any P wave—form the basis of our interpretation of the foreshock event as a VLFE. The signals of both the earthquake and the VLFE were strongly

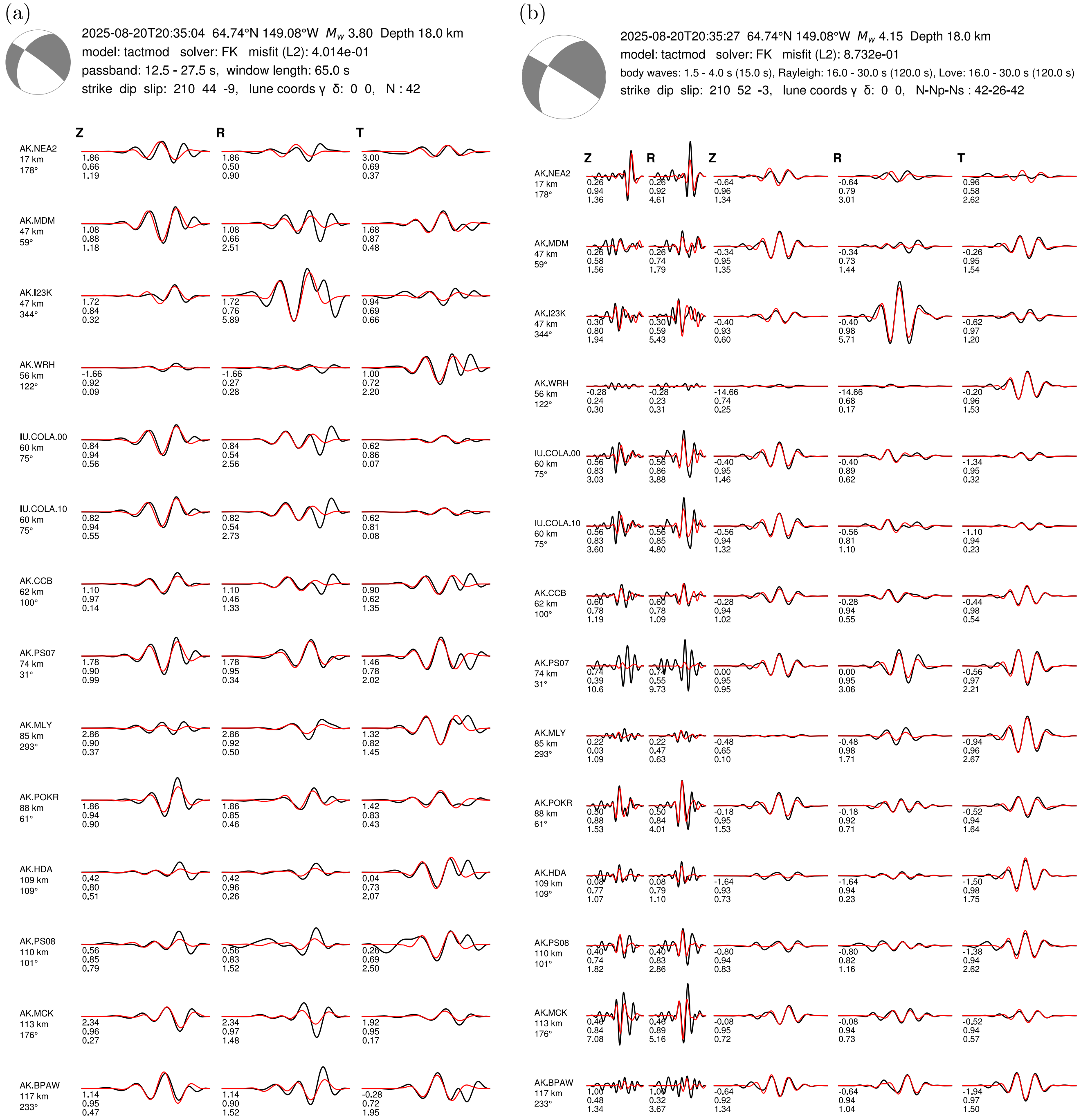

Figure 2. Source mechanism and waveform fits for the 2025 VLFE and the 2025 earthquake that occurred 23.6 s after the VLFE. Refer to Thurin et al. (2025) for details on figure headers. (a) 2025 VLFE. The waveforms are displayed for three components (Z vertical, R radial, T transverse) for data (black) and synthetics (red), both filtered between periods 12.5–27.5 s. Waveform fits from 41 stations were used in the inversion; displayed here are the 13 closest stations, all within 120 km of the epicenter. (b) 2025 earthquake. For this inversion, P waves (Z and R components) were used in addition to surface waves (Z, R, T).

dependent on the choice of bandpass, and therefore we performed a large number of moment tensor estimations using a set of 55 different pass bands defined by periods between 2.5 and 40.0 s in increments of 2.5 s. The results (Figure S4 in Supporting Information S1) identified an optimal bandpass of 12.5–27.5 s (0.036–0.080 Hz) for the VLFE, and they also showed that the moment tensors did not depend significantly on the choice of bandpass.

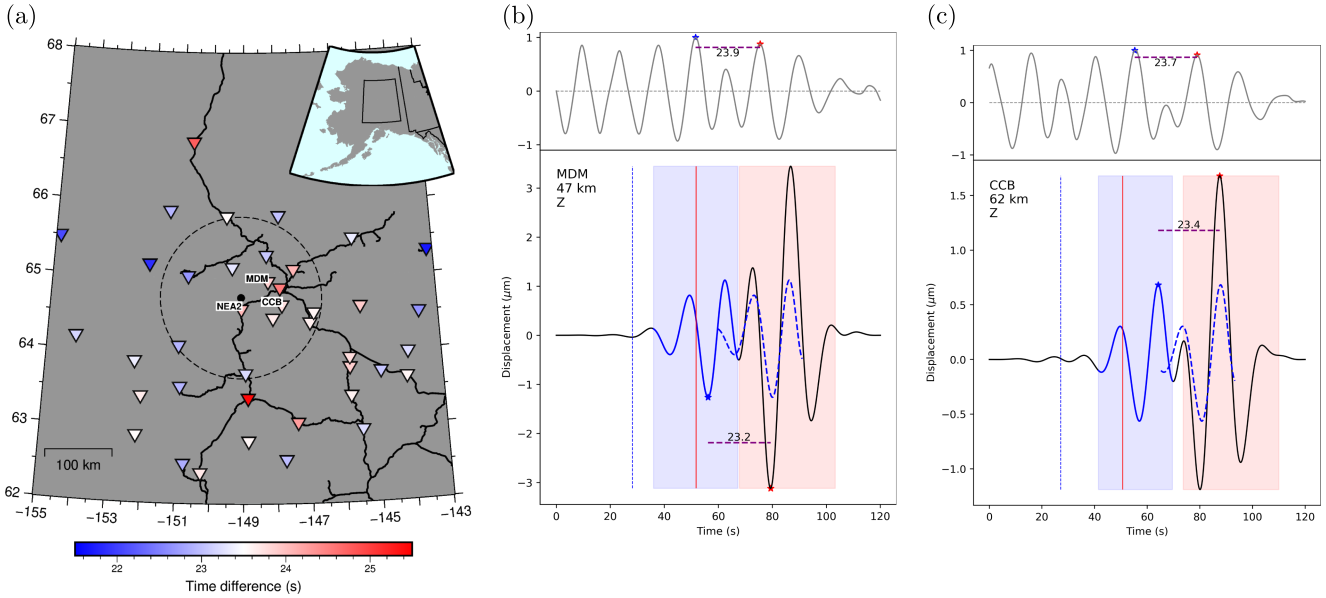

Figure 3. Determination of ΔT_{cc}, which is the time shift associated with our interpreted alignment between the VLFE waveform and the earthquake waveform. With the assumption of collocated hypocenters for the VLFE and earthquake, ΔT_{cc} is the earthquake origin time minus the VLFE origin time. (a) Summary map of ΔT_{cc} measurements. The dashed circle, with epicentral radius 120 km, encloses 13 stations used to calculate the mean value of 23.6 s. (b) Recorded waveform for example, station MDM, vertical component, filtered 12.5–27.5 s; its location is labeled in panel (a). In the lower subplot, the blue window is the VLFE, the red window is the earthquake. The upper subplot shows the cross-correlation (CC) value obtained by sliding the VLFE waveform across the full seismogram; the blue star marks self-alignment, and the red star marks the interpreted alignment with the designated earthquake waveform. The CC-determined value is generally very close to the time shift between peaks, depicted by the horizontal bar in the lower plot. The optimally shifted VLFE waveform is plotted in dashed blue. The red vertical line is the catalog P pick for the earthquake, the blue dashed line is 23.6 s earlier, representing the hypothetical P arrival for the VLFE. (c) Example station CCB. A complete set of plots is provided in the Supplement (Figures S8–S12 in Supporting Information S1).

The estimated moment tensors and waveform fits for the 2025 VLFE and earthquake are shown in Figure 2. The VLFE is smaller: M_w 3.80 versus M_w 4.15. The most striking feature is the similarity between the earthquake mechanism (Figure 2b) and the VLFE mechanism (Figure 2a): the minimum angle between the two mechanisms is only 8°.

The similarity of the VLFE and earthquake mechanisms prompted additional efforts to quantify the timing between these events (Figures S5 and S6 in Supporting Information S1). Given that the 2025 earthquake and VLFE hypocenters are very close and given that moment tensors are very similar, it should be possible to identify the relative time between these two events by carefully examining low-frequency waveforms.

Figure 3 presents a data-only perspective on the earthquake and VLFE signals. For each of the 41 stations used to estimate the VLFE mechanism, we chose one of the three components (Z, R, T) and identified two time windows that best contained the VLFE and earthquake waveforms. We then cross-correlated the VLFE waveform with the full-length waveform, which reveals an oscillatory function having a maximum value of 1 (when the VLFE is aligned with itself) and a high value associated with optimal alignment between the VLFE waveform and the earthquake waveform. For the two example stations in Figure 3, the differential time between VLFE and earthquake waveforms is 23.9 s (MDM) and 23.7 s (CCB). The differential times for all 41 stations are displayed in Figure 3a. Using the closest 13 stations within 120 km of the epicenter, we calculate a mean value of 23.6 ± 0.5 s. The lack of a pronounced spatial pattern of differential times (Figure 3a) indicates that the VLFE and earthquake epicenters are close to each other, which, combined with the similarities in depths (17.2 km vs. 18.6 km: Figure S3 in Supporting Information S1), led us to model the VLFE with the same hypocenter as the earthquake. Using the value of 23.6 s (Figure 3a) and the origin time of the earthquake, we directly determine the VLFE origin time (Table 1).

Closer inspection of the differential times in Figure 3a shows that they are slightly larger to the east (24 s) than to the west (23 s), suggesting that the VLFE is offset to the southeast from the earthquake (Figure S13 in Supporting Information S1). However, a more rigorous analysis would need to take into account the extreme 3D structural variations in this region (Tape et al., 2015; Van Kooten et al., 2012) and consider modeling the high-frequency waveforms (e.g., Hawthorne & Ampuero, 2017). Based on the low-frequency analysis in Figure S13 in Supporting Information S1, we consider the VLFE to be 0–2 km from the earthquake. For comparison, the approximate source dimension for a M_w 4 event is 1.3 km, assuming a stress drop of 2 MPa.

2.2. High-Frequency Analysis of the 2025 Events

The high-frequency waveforms for the 2025 events provide important context for the low-frequency signals. Figure 4a displays waveforms for a comparison earthquake: 2022 M_w 4.5 (Figure 1). Two versions of the vertical-component waveform at NEA2 are shown: high-frequency and low-frequency. The low-frequency seismogram is causally (one-pass) filtered, which is why the low-frequency waves begin after the high-frequency P onset (at $t = 0$).

The same filtering is then applied to the 2025 event, shown in Figure 4b. Two differences from the 2022 earthquake signal are apparent: (a) there are pre-P high-frequency waveforms, and (b) there are pre-P low-frequency waveforms. Extracting a 60 s portion of Figure 4b, we obtain Figure 4c, which sets the stage for the timeline of the 2025 event.

The HFF signal originated at 2025-08-20 20:34:45.2, represented by the left limit of the x-axis in Figure 4c. 3.4 s later, the waves reach station NEA2, 15 km from the HFF epicenter and 21 km from the hypocenter. This marks the start of the HFF signal, which lasts for 19.4 s (light blue shading) before being joined by the VLFE (light purple shading). The VLFE extends 24.3 s, at which point the M_w 4.2 earthquake occurs. Thus, the three colors define the three main episodes of the 2025 event: HFF (blue), VLFE + HFF (purple), and earthquake (red). Similar waveforms to those at NEA2 (Figure 4c) can be seen at all 41 stations examined in this study. Considering all measurements, the durations of the precursory stages are 18.9 s (HFF) and 23.6 s (VLFE + HFF), for a total of 42.5 s of precursory signals.

How did the 2025 event start? What is clear is that it did not start with an impulsive P wave. It begins with an emergent HFF signal, 42.5 s before the M_w 4.2 earthquake. The inset of Figure 4c displays the onset of the HFF signal for one example station (NEA2); others can be found in Figure S15 of Supporting Information S1. Qualitatively, there are no coherent waveforms among recordings at the 13 closest stations. Zooming into the first waves to emerge from each station's background noise level, we cannot discern any coherent waveform. Waveform coherence emerges after 18.9 s, with the low-frequency M_w 3.8 VLFE.

3. Discussion and Conclusions

This study documents an earthquake immediately preceded by a VLFE having nearly the same mechanism as the earthquake. The VLFE occurs within a HFF signal lasting 42.5 s in total, indicating 18.9 s of HFF prior to the occurrence of the VLFE. In the context of previous activity in Minto Flats fault zone (Tape et al., 2018), the 2025 event provides the best-documented example of a VLFE associated with earthquake initiation. In contrast to the 2016 MFFZ event, for which low-frequency signals were weak and difficult to resolve, the 2025 sequence provides well-constrained timing, location, and source properties for both the VLFE and the subsequent earthquake.

The 2025 event exhibits three stages depicted by colors in Figure 4c: HFF signal, VLFE, and earthquake. The close agreement in location (separated by 0–2 km), timing (23.6 s apart), and moment tensors between the VLFE and the earthquake strongly suggests a causal relationship. The absence of a clear P wave for the VLFE indicates that slip occurred slowly relative to seismic rupture, consistent with a slow-slip process. The accompanying high-frequency energy can be interpreted as radiation from localized brittle failure at the margins of the slipping region, similar to patterns inferred in earlier MFFZ events (Tape et al., 2018; Figure 4a). These observations indicate that slow slip and seismic radiation coexist during the initiation process and that the VLFE marks a transitional stage between aseismic deformation and dynamic rupture.

The tectonic setting of the Minto Flats fault zone provides important context for this behavior. The prevailing tectonic perspective of the central Alaska fault zones, including MFFZ, is that they form bookshelf faulting (Page et al., 1995): northeast-striking left-lateral strike-slip faults situated between the two larger-scale right-lateral strike-slip fault systems of Denali (south) and Kaltag-Tintina (north). The MFFZ has two main faults (MFFZ-W, MFFZ-E: Figure 1) that are offset and form a transtensional setting, with Nenana basin between the two main

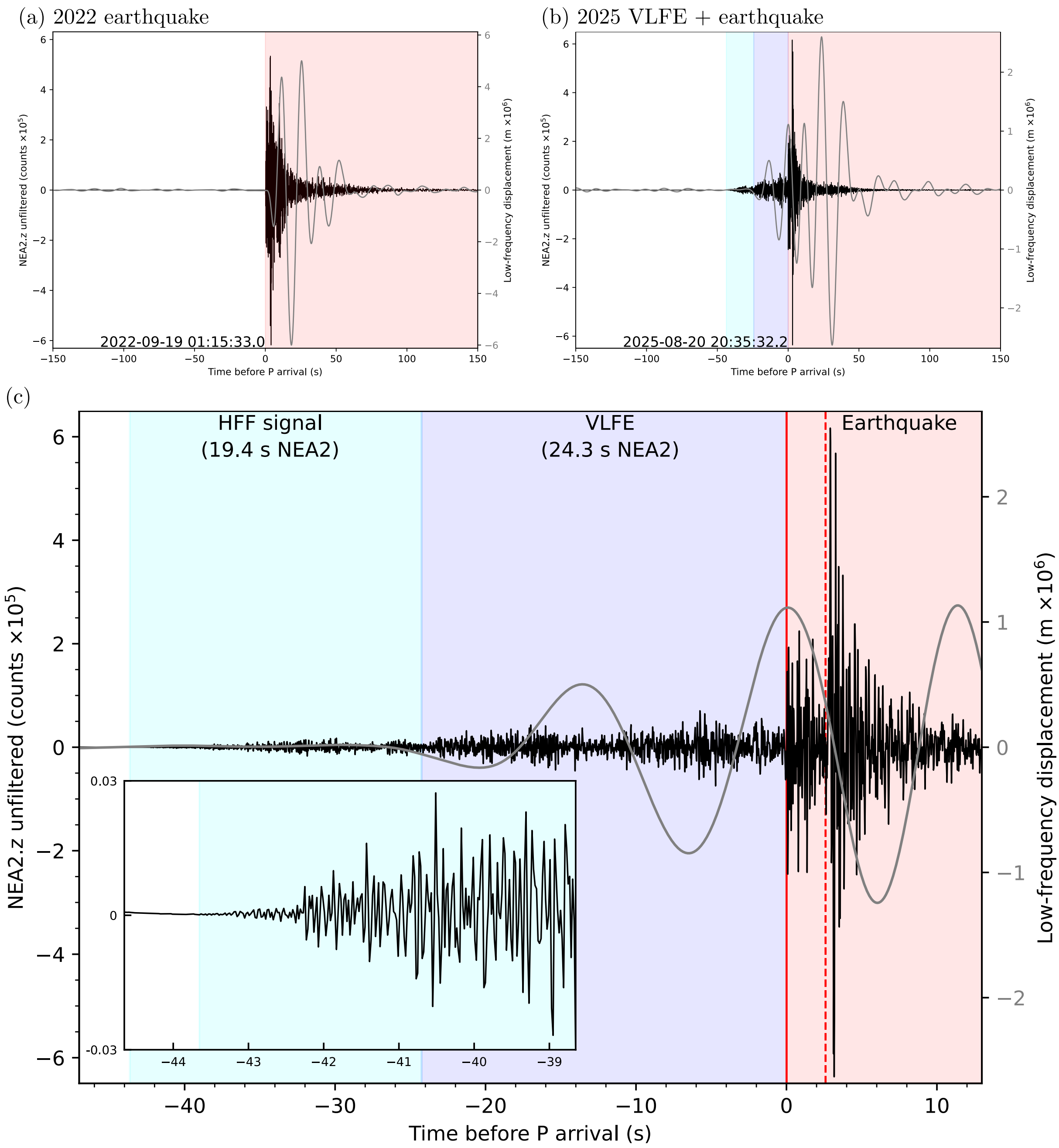

Figure 4. Seismic recordings at station NEA2, which is at an epicentral distance of 15 km. In each plot, two seismograms are displayed. One (black) is the unfiltered seismogram, the other (gray) is causally filtered between periods 12.5–27.5 s (a) 2022 M_{w} 4.5 earthquake. The time axis is referenced and centered on the P arrival at $t = 0$; the absolute time is listed at the bottom. (b) 2025 VLFE + earthquake. The signals prior to the P onset at $t = 0$ represent the VLFE. (c) Zoom-in on (b), showing the three stages of the event: HFF signal, VLFE + HFF signal, and earthquake. The x-axis limit of $t = -47.0$ s is the HFF origin time. The inset plot displays the first 5 s of the high-frequency signal; the y-limits are ±3000 counts. The blue stage starts at $t = -43.7$ s, which is the duration of precursory signals recorded at NEA2.

faults (Tape et al., 2015). Recent enhanced and relocated seismicity catalogs reveal a more complex picture of MFFZ (Figure 1) that includes conjugate faulting as well as northwest-dipping faults between MFFZ-W and MFFZ-E and directly below Nenana basin (Sims et al., 2026). The moment tensors for the 2025 events (Figure 2) are consistent with left-lateral slip on a northeast-striking fault dipping to the northwest, at depths of approximately 18 km (Figure 1). In this context, the relative differences in depths and epicenters suggest that the VLFE occurred updip, southeast, and adjacent to the earthquake.

A future analysis using phase coherence of high-frequency waveforms (Figure S15 in Supporting Information S1) could help identify microsources, as demonstrated by Hawthorne and Ampuero (2017) and Tape et al. (2018) for events in Minto Flats fault zone. Such an analysis could provide a better estimate of the relative distance between the 2025 VLFE and the following earthquake. These high-frequency waves could also be used to estimate a source-time function, as done by Tape et al. (2018) for a VLFE in 2015.

By considering the source duration as an inversion parameter, we were able to further distinguish the 2025 VLFE from the earthquake. The preferred duration for the M_w 4.2 earthquake is $\leq$ 1.0 s, while the preferred duration for the M_w 3.8 VLFE is 8.0 s (Figure S18 in Supporting Information S1). The low-frequency signals are best explained by a VLFE initiating 24 s before the earthquake with an effective duration of ∼8 s, leaving a gap of roughly 16 s that may have included aseismic or low-amplitude slip. The moment and duration of this VLFE fall between the slow and fast earthquake scaling trends (Figure S19 in Supporting Information S1; Ide & Beroza, 2023) and lie just outside the lower bound of previously reported VLFEs in subduction zones (Takemura et al., 2019), suggesting that such events are relatively rare in nature and may represent a slow-to-fast transitional rupture.

The 2025 event further supports the conditions of MFFZ that produce VLFEs and earthquakes with initiation signals (Tape et al., 2018): magnitudes M_w 3.5–4.2, strike-slip faulting, and lower-crustal depths of 17–23 km. These observations reinforce the view that the lower crust beneath the MFFZ favors mixed-mode faulting and repeated initiation behavior. From the 2025 VLFE and earthquake mechanisms, the inferred southwest-directed motion of the northwest fault block above 18 km is potentially related to the eastern extent of proposed crustal extrusion of southwestern Alaska (Cross & Freymueller, 2008; Redfield et al., 2007).

The observed sequence of high-frequency activity, VLFE, and dynamic rupture can be interpreted within several conceptual frameworks, including two end-member scenarios. In one scenario, a slow aseismic slip front propagates along the fault and intermittently generates microseismicity, while the accompanying slow slip manifests as a VLFE that ultimately nucleates the earthquake (Tape et al., 2018). In the other end-member scenario, the signals preceding the mainshock arise from clustered microearthquakes, with the high-frequency component generated by individual small events and the apparent VLFE representing the long-period superposition of their S waves rather than a distinct slow-slip episode (Gomberg et al., 2016; Ide, 2008). Between these end members, the VLFE may arise from a mixture of seismic and aseismic slip on a fault with heterogeneous frictional properties (Ando et al., 2012; R. Ito & Kaneko, 2023), causing the rupture to propagate slowly through repeated acceleration and deceleration and thereby producing a long-duration event. Future numerical modeling informed by our observations will be important for distinguishing among these possibilities and advancing understanding of the physical mechanisms governing slow-to-fast rupture transitions.

Regardless of the underlying slip process, the 2025 MFFZ event provides one of the clearest observational links between slow deformation and earthquake initiation yet documented. The detailed temporal resolution, spatial coherence, and similarity of moment tensors between the VLFE and the earthquake place strong constraints on models of nucleation. Together with previous MFFZ events, these observations highlight the value of this fault system as a natural laboratory for studying interactions between slow and fast deformation processes during earthquake initiation.

Conflict of Interest

The authors declare no conflicts of interest relevant to this study.

Availability Statement

All waveforms used in this study are accessible from the EarthScope Data Management Center. We used a subset of stations from the following seismic networks: AK (AEC, 1987), XV (Tape & West, 2014), TA (IRIS Transportable Array, 2003), and IU (ASL, 1988). We estimated moment tensors using the open-source software package MTUQ (Thurin et al., 2025). A complete set of results is provided in McPherson (2025).

Acknowledgments

We thank three anonymous reviewers for their detailed and constructive feedback. This project was supported by National Science Foundation Grant EAR 2342129, the TREMOR project funded by Air Force Research Laboratory contract FA9453-24-9-0001, and JSPS KAKENHI (21H05206). We thank Aakash Gupta for his initial source estimations and discussions. We thank AEC seismic data analyst Derreck Gossett and seismic data manager Heather McFarlin for their analysis and review of the 2025 events (Table 1). We thank Julien Thurin for supporting MTUQ software and Bryant Chow for supporting PySEP software.

References

AEC. (1987). *Alaska Geophysical Network*. Alaska Earthquake Center (AEC), Univ. of Alaska Fairbanks. International Federation of Digital Seismograph Networks. https://doi.org/10.7914/SN/AK

Ando, R., Takeda, N., & Yamashita, T. (2012). Propagation dynamics of seismic and aseismic slip governed by fault heterogeneity and Newtonian rheology. *Journal of Geophysical Research*, *117*(B11). https://doi.org/10.1029/2012jb009532

ASL. (1988). *Global Seismograph Network—IRIS/USGS*. Albuquerque Seismological Laboratory (ASL)/USGS. International Federation of Digital Seismograph Networks. https://doi.org/10.7914/SN/IU

Beaudoin, B. C., Fuis, G. S., Mooney, W. D., Nokleberg, W. J., & Christensen, N. I. (1992). Thin, low-velocity crust beneath the southern Yukon-Tanana terrane, east central Alaska: Results from Trans-Alaska Crustal Transect refraction/wide-angle reflection data. *Journal of Geophysical Research*, *97*(B2), 1921–1942. https://doi.org/10.1029/91jb02881

Beroza, G. C., & Ellsworth, W. L. (1996). Properties of the seismic nucleation phase. *Tectonophysics*, *261*(1–3), 209–227. https://doi.org/10.1016/0040-1951(96)00067-4

Bouchon, M., Karabulut, H., Aktar, M., Özalaybey, S., Schmittbuhl, J., & Bouin, M.-P. (2011). Extended nucleation of the 1999 M_w 7.6 Izmit earthquake. *Science*, *331*(6019), 877–880. https://doi.org/10.1126/science.1197341

Cattania, C., & Segall, P. (2021). Precursory slow slip and foreshocks on rough faults. *Journal of Geophysical Research: Solid Earth*, *126*(4), e2020JB020430. https://doi.org/10.1029/2020JB020430

Cross, R. S., & Freymueller, J. T. (2008). Evidence for and implications of a Bering plate based on geodetic measurements from the Aleutians and western Alaska. *Journal of Geophysical Research*, *113*(B7), 1–19. https://doi.org/10.1029/2007JB005136

Dieterich, J. H. (1992). Earthquake nucleation on faults with rate- and state-dependent strength. *Tectonophysics*, *211*(1–4), 115–134. https://doi.org/10.1016/0040-1951(92)90055-b

Ellsworth, W. L., & Beroza, G. C. (1995). Seismic evidence for an earthquake nucleation phase. *Science*, *268*(5212), 851–855. https://doi.org/10.1126/science.268.5212.851

Ellsworth, W. L., & Bulut, F. (2018). Nucleation of the 1999 Izmit earthquake by a triggered cascade of foreshocks. *Nature Geoscience*, *11*(7), 531–535. https://doi.org/10.1038/s41561-018-0145-1

Gomberg, J. (2018). Unsettled earthquake nucleation. *Nature Geoscience*, *11*(7), 463–464. https://doi.org/10.1038/s41561-018-0149-x

Gomberg, J., Agnew, D. C., & Schwartz, S. Y. (2016). Alternative source models of very low frequency events. *Journal of Geophysical Research: Solid Earth*, *121*(9), 6722–6740. https://doi.org/10.1002/2016JB013001

Hawthorne, J. C., & Ampuero, J.-P. (2017). A phase coherence approach to identifying co-located earthquakes and tremor. *Geophysical Journal International*, *209*, 623–642. https://doi.org/10.1093/gji/ggx012

Ide, S. (2008). A Brownian walk model for slow earthquakes. *Geophysical Research Letters*, *35*(17). https://doi.org/10.1029/2008GL034821

Ide, S., & Beroza, G. C. (2023). Slow earthquake scaling reconsidered as a boundary between distinct modes of rupture propagation. *Proceedings of the National Academy of Sciences*, *120*(32), 1–7. https://doi.org/10.1073/pnas.2222102120

Iio, Y. (1995). Observations of the slow initial phase generated by microearthquakes: Implications for earthquake nucleation and propagation. *Journal of Geophysical Research*, *100*(B8), 15333–15349. https://doi.org/10.1029/95jb01150

IRIS Transportable Array. (2003). *USArray Transportable Array*. International Federation of Digital Seismograph Networks. https://doi.org/10.7914/SN/TA

Ito, R., & Kaneko, Y. (2023). Physical mechanism for a temporal decrease of the Gutenberg-Richter b-value prior to a large earthquake. *Journal of Geophysical Research: Solid Earth*, *128*(12), 1–21. https://doi.org/10.1029/2023JB027413

Ito, Y., Hino, R., Kido, M., Fujimoto, H., Osada, Y., Inazu, D., et al. (2013). Episodic slow slip events in the Japan subduction zone before the 2011 Tohoku-Oki earthquake. *Tectonophysics*, *600*, 14–26. https://doi.org/10.1016/j.tecto.2012.08.022

Kaneko, Y., Nielsen, S. B., & Carpenter, B. M. (2016). The onset of laboratory earthquakes explained by nucleating rupture on a rate-and-state fault. *Journal of Geophysical Research: Solid Earth*, *121*(8), 6071–6091. https://doi.org/10.1002/2016JB013143

Kato, A., & Ben-Zion, Y. (2021). The generation of large earthquakes. *Nature Reviews Earth & Environment*, *2*(1), 26–39. https://doi.org/10.1038/s43017-020-00108-w

Kato, A., Obara, K., Igarashi, T., Tsuruoka, H., Nakagawa, S., & Hirata, N. (2012). Propagation of slow slip leading up to the 2011 M_w 9.0 Tohoku-Oki earthquake. *Science*, *335*(6069), 705–708. https://doi.org/10.1126/science.1215141

Latour, S., Schubnel, A., Nielsen, S., Madariaga, R., & Vinciguerra, S. (2013). Characterization of nucleation during laboratory earthquakes. *Geophysical Research Letters*, *40*(19), 5064–5069. https://doi.org/10.1002/grl.50974

Martínez-Garzón, P., & Poli, P. (2024). Cascade and pre-slip models oversimplify the complexity of earthquake preparation. *Nature*, *5*, 1–13. https://doi.org/10.1038/s43247-024-01285-y

McClaskey, G. (2019). Earthquake initiation from laboratory observations and implications for foreshocks. *Journal of Geophysical Research: Solid Earth*, *124*, 12882–12904. https://doi.org/10.1029/2019JB018363

McPherson, A. M. (2025). Seismic moment tensor results in support of “Observational evidence of a very-low-frequency earthquake (Mw 3.8) leading to an earthquake (Mw 4.2): Minto Flats strike-slip fault zone, central Alaska” [Dataset]. *Zenodo*. https://doi.org/10.5281/zenodo.18039187

Mori, J., & Kanamori, H. (1996). Initial rupture of earthquakes in the 1995 Ridgecrest, California sequence. *Geophysical Research Letters*, *23*(18), 2437–2440. https://doi.org/10.1029/96gl02491

Ohnaka, M., & Shen, L.-F. (1999). Scaling of the shear rupture process from nucleation to dynamic propagation: Implications of geometric irregularity of the rupturing surfaces. *Journal of Geophysical Research*, *104*(B1), 817–844. https://doi.org/10.1029/1998JB900007

Page, R. A., Plafker, G., & Pulpan, H. (1995). Block rotation in east-central Alaska: A framework for evaluating earthquake potential? *Geology*, *23*(7), 629–632. https://doi.org/10.1130/0091-7613(1995)023<0629:brieca>2.3.co;2

Peng, Z., & Lei, X. (2025). Physical mechanisms of earthquake nucleation and foreshocks: Cascade triggering, aseismic slip, or fluid flows? *Earthquake Research Advances*, *5*(2), 1–16. https://doi.org/10.1016/j.eqrea.2024.100349

Ratchkovski, N. A., & Hansen, R. A. (2002). New constraints on tectonics of interior Alaska: Earthquake locations, source mechanisms, and stress regime., *92*(3), 998–1014. https://doi.org/10.1785/0120010182

Redfield, T. F., Scholl, D. W., Fitzgerald, P. G., & Beck, M. E., Jr. (2007). Escape tectonics and the extrusion of Alaska: Past, present, and future. *Geology*, *35*(11), 1039–1042. https://doi.org/10.1130/g23799a.1

Rubin, A. M., & Ampuero, J.-P. (2005). Earthquake nucleation on (aging) rate and state faults. *Journal of Geophysical Research*, *110*(B11). https://doi.org/10.1029/2005JB003686

Ruiz, S., Metois, M., Fuenzalida, A., Ruiz, J., Leyton, F., Grandin, R., et al. (2014). Intense foreshocks and a slow slip event preceded the 2014 Iquique M_w 8.1 earthquake. *Science*, *345*(6201), 1165–1169. https://doi.org/10.1126/science.1256074

Schurr, B., Asch, G., Hainzl, S., Bedford, J., Hoechner, A., Palo, M., et al. (2014). Gradual unlocking of plate boundary controlled initiation of the 2014 Iquique earthquake. *Nature*, *512*(7514), 299–302. https://doi.org/10.1038/nature13681

Silwal, V., & Tape, C. (2016). Seismic moment tensors and estimated uncertainties in southern Alaska. *Journal of Geophysical Research: Solid Earth*, *121*(4), 2772–2797. https://doi.org/10.1002/2015JB012588

Sims, N. E., Tape, C., Ruppert, N. A., & West, M. E. (2026). High-precision earthquake catalog for Minto Flats fault zone, central Alaska, reveals complex and conjugate faulting. *Bulletin of the Seismological Society of America*, *116*(1), 375–396. https://doi.org/10.1785/0120250177

Smith, K., Tape, C., & Tsai, V. C. (2023). Seismic response of Nenana sedimentary basin, central Alaska. *Bulletin of the Seismological Society of America*, *113*(2), 762–781. https://doi.org/10.1785/0120220160

Takemura, S., Matsuzawa, T., Noda, A., Tonegawa, T., Asano, Y., Kimura, T., & Shiomi, K. (2019). Structural characteristics of the Nankai Trough shallow plate boundary inferred from shallow very low frequency earthquakes. *Geophysical Research Letters*, *46*(8), 4192–4201. https://doi.org/10.1029/2019GL082448

Tape, C., Holtkamp, S., Silwal, V., Hawthorne, J., Kaneko, Y., Ampuero, J. P., et al. (2018). Earthquake nucleation and fault slip complexity in the lower crust of central Alaska. *Nature Geoscience*, *11*(7), 536–541. https://doi.org/10.1038/s41561-018-0144-2

Tape, C., Silwal, V., Ji, C., Keyson, L., West, M. E., & Ruppert, N. (2015). Transtensional tectonics of the Minto Flats fault zone and Nenana basin, central Alaska. *Bulletin of the Seismological Society of America*, *105*(4), 2081–2100. https://doi.org/10.1785/0120150055

Tape, C., West, M., Silwal, V., & Ruppert, N. (2013). Earthquake nucleation and triggering on an optimally oriented fault. *Earth and Planetary Science Letters*, *363*, 231–241. https://doi.org/10.1016/j.epsl.2012.11.060

Tape, C., & West, M. E. (2014). *Fault Locations and Alaska Tectonics from Seismicity*. International Federation of Digital Seismograph Networks. https://doi.org/10.7914/SN/XV_2014

Thurin, J., Modrak, R., Tape, C., McPherson, A. M., Rodríguez-Cardozo, F. R., Kintner, J., et al. (2025). MTUQ: A framework for estimating moment tensors, point forces, and their uncertainties. *Geophysical Journal International*, *241*(2), 1373–1390. https://doi.org/10.1093/gji/ggaf080

Van Kooten, G. K., Richter, M., & Zippi, P. A. (2012). Alaska's Interior rift basins: A new frontier for discovery. *Oil & Gas Journal*, *110*(1a), 48–57.

Yabe, S., & Ide, S. (2018). Variations in precursory slip behavior resulting from frictional heterogeneity. *Progress in Earth and Planetary Science*, *5*(1), 1–11. https://doi.org/10.1186/s40645-018-0201-x

Yamashita, F., Fukuyama, E., Xu, S., Kawakata, H., Mizoguchi, K., & Takizawa, S. (2021). Two end-member earthquake preparations illuminated by foreshock activity on a meter-scale laboratory fault. *Nature Communications*, *12*(1), 4302. https://doi.org/10.1038/s41467-021-24625-4

Zhao, L.-S., & Helmberger, D. V. (1994). Source estimation from broadband regional seismograms. *Bulletin of the Seismological Society of America*, *84*(1), 91–104. https://doi.org/10.1785/BSSA0840010091

Zhu, L., & Helmberger, D. (1996). Advancement in source estimation techniques using broadband regional seismograms. *Bulletin of the Seismological Society of America*, *86*(5), 1634–1641. https://doi.org/10.1785/bssa0860051634

Supporting Information for "Observational evidence of a very-low-frequency earthquake (M_{w} 3.8) leading to an earthquake (M_{w} 4.2): Minto Flats strike-slip fault zone, central Alaska"

A. M. McPherson, C. Tape, Y. Kaneko

Contents of this file

1. Text S1 to S2
2. Table S1
3. Figures S1 to S19

S1. Moment tensor estimation for the 2025 events

The similarity of the VLFE and earthquake moment tensors (Figure 2) prompted additional efforts to quantify the timing between these events and to elucidate the influence of different choices within the estimation procedure. Using wider time windows containing both the VLFE and earthquake arrivals, filtered 12.5–27.5 s, we estimated both moment tensors by only changing the allowable time shifts. The origin time used is the high-frequency foreshock (HFF) event in the catalog (2025-08-20 20:34:45.2). In Figure S5a, we allow ±30 s time shifts between data and synthetics; the best-fitting moment tensor is that of the VLFE, and we can see that the synthetic waveforms align with the early, lower-amplitude portion of the observed waveforms. In Figure S5b, we allow ±50 s time shifts between data and synthetics; the best-fitting moment tensor is that of the earthquake, and we can see that the synthetic waveforms align with the later, high-amplitude portion of the observed waveforms. Thus, by changing only the allowable time shift limits, we estimate either the VLFE or the earthquake.

Figure S6 provides a one-to-one comparison of the VLFE and earthquake moment tensor estimation, where the same stations and time windows (stations, window length, and Z/R/T) have been selected. In these cases, as well as within the full suite of inversions depicted by Figure S4, the window lengths are 65 s, which is chosen to minimize the interference of the (later) earthquake waveforms with the (earlier) VLFE waveforms, while also capturing at least one cycle of the longest allowable period (40 s) within all bandpasses. The start and end times of the time windows are based on the assumed 1D velocity model, using the default settings in MTUQ (Thurin et al., 2025). The allowable time shifts are specified to the relatively small value of ±3.0 s, in order to minimize cycle-skipping while also accommodating deficiencies of the 1D Earth model in modeling the true Earth structure. In estimating the 2025 VLFE moment tensor, the factors listed in order from most to least importance, are: 1) the origin time derived from the low-frequency waveforms (20:35:04.1), 2) the allowable time shifts, 3) the bandpass (e.g., Figure S4), and 4) the window length.

Full results for the moment tensor estimations can be found in McPherson (2025).

S2. High-frequency record sections

The waveforms at the start of each event are captured by the high-frequency record sections in Figures S15–S17. These waveforms are unfiltered, with units of counts. The 2025 VLFE onset (Fig. S15a) is emergent on all stations. The 2025 earthquake onset (Fig. S15b) has a clear P wave at some stations (I23K, NEA2, POKR), but it is complicated by the pre-P signal arising from the preceding VLFE. By comparison, there is no visible signal prior to the P wave at the reference earthquakes in 2019 (Fig. S16) and 2022 (Fig. S17).

References

Ide, S., & Beroza, G. C. (2023). Slow earthquake scaling reconsidered as a boundary between distinct modes of rupture propagation. *Proc. Natl. Acad. Sci.*, *120*(32), 1–7. doi: 10.1073/pnas.2222102120

McPherson, A. (2025). *Seismic moment tensor results in support of "Observational evidence of a very-low-frequency earthquake (M_{w} 3.8) leading to an earthquake (M_{w} 4.2): Minto Flats strike-slip fault zone, central Alaska".* ([Data set]. Zenodo `https://doi.org/10.5281/zenodo.18039187`)

Takemura, S., Matsuzawa, T., Noda, A., Tonegawa, T., Asano, Y., Kimura, T., & Shiomi, K. (2019). Structural characteristics of the Nankai Trough shallow plate boundary inferred from shallow very low frequency earthquakes. *Geophys. Res. Lett.*, *46*, 4192–4201. doi: 10.1029/2019GL082448

Tape, C., Holtkamp, S., Silwal, V., Hawthorne, J., Kaneko, Y., Ampuero, J. P., ... West, M. E. (2018). Earthquake nucleation and fault slip complexity in the lower crust of central Alaska. *Nature Geoscience*, *11*, 536–541. doi: 10.1038/s41561-018-0144-2

Thurin, J., Modrak, R., Tape, C., McPherson, A., Rodríguez-Cardozo, F. R., Kintner, J., ... Braunmiller, J. (2025). MTUQ: a framework for estimating moment tensors, point forces, and their uncertainties. *Geophys. J. Int.*, *241*, 1373–1390. doi: 10.1093/gji/ggaf080

0148-0227/26/$9.00

Table S1: Sources mechanisms estimated in this study. Origin times and epicenters are listed in Table 1. Figure 1 displays these mechanisms. SW = surface wave. The depth in parentheses is the best-fitting depth, which in some cases differs from the depth chosen for the study.

ID	Event	Magnitude (M_w)	Depth (km)	P wave bandpass	SW bandpass	Fault 1 strike/dip/rake	Fault 2 strike/dip/rake
M1	2015 earthquake	2.85	21 (21)	0.7–2.5 Hz	–	210/28/-15	313/83/-117
M2	2019 earthquake	4.20	14 (14)	1.5–4.0 s	16–30 s	198/70/-9	291/82/-159
M3	2022 earthquake	4.50	15 (15)	1.5–4.0 s	16–30 s	186/83/-39	281/51/-171
M4	2025 earthquake	4.15	18 (19)	1.5–4.0 s	16–30 s	210/52/-3	302/88/-142
M5	2025 earthquake [P only]	4.15	18 (18)	1.5–4.0 s	–	210/54/-3	302/88/-144
M6	2025 earthquake [SW only]	4.25	26 (26)	–	16–30 s	210/54/-9	305/83/-144
M7	2025 earthquake [SW only]	4.10	18 (13)	–	12.5–27.5 s	210/52/-9	306/83/-142
M8	2025 VLFE	3.80	18 (17)	–	12.5–27.5 s	210/44/-9	306/84/-142

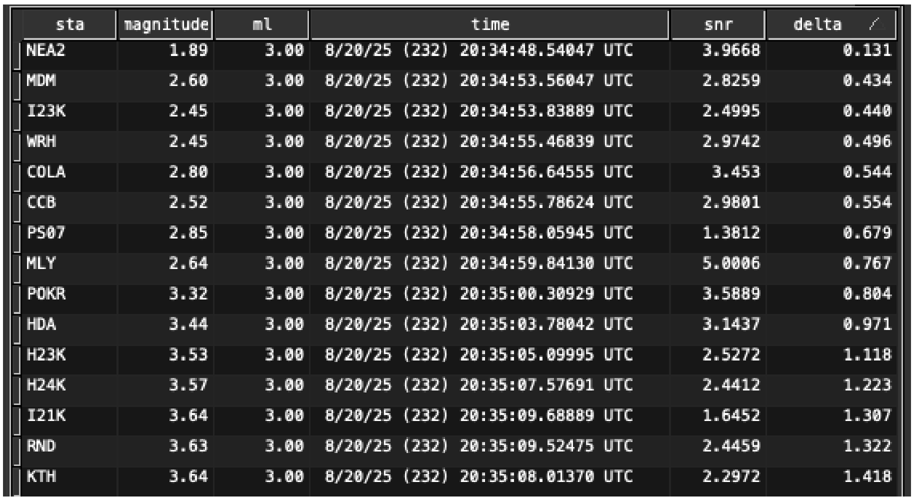

sta	magnitude	ml	time	snr	delta
NEA2	1.89	3.00	8/20/25 (232) 20:34:48.54047 UTC	3.9668	0.131
MDM	2.60	3.00	8/20/25 (232) 20:34:53.56047 UTC	2.8259	0.434
I23K	2.45	3.00	8/20/25 (232) 20:34:53.83889 UTC	2.4995	0.440
WRH	2.45	3.00	8/20/25 (232) 20:34:55.46839 UTC	2.9742	0.496
COLA	2.80	3.00	8/20/25 (232) 20:34:56.64555 UTC	3.453	0.544
CCB	2.52	3.00	8/20/25 (232) 20:34:55.78624 UTC	2.9801	0.554
PS07	2.85	3.00	8/20/25 (232) 20:34:58.05945 UTC	1.3812	0.679
MLY	2.64	3.00	8/20/25 (232) 20:34:59.84130 UTC	5.0006	0.767
POKR	3.32	3.00	8/20/25 (232) 20:35:00.30929 UTC	3.5889	0.804
HDA	3.44	3.00	8/20/25 (232) 20:35:03.78042 UTC	3.1437	0.971
H23K	3.53	3.00	8/20/25 (232) 20:35:05.09995 UTC	2.5272	1.118
H24K	3.57	3.00	8/20/25 (232) 20:35:07.57691 UTC	2.4412	1.223
I21K	3.64	3.00	8/20/25 (232) 20:35:09.68889 UTC	1.6452	1.307
RND	3.63	3.00	8/20/25 (232) 20:35:09.52475 UTC	2.4459	1.322
KTH	3.64	3.00	8/20/25 (232) 20:35:08.01370 UTC	2.2972	1.418

Figure S1: Screenshot provided by Alaska Earthquake Center seismologists, showing the single-station magnitude (M_L: 2nd column) estimates for the 2025 high-frequency foreshock signal. The columns are: station, single-station magnitude (M_L), event magnitude (M_L), P onset time, signal-to-noise ratio, and epicenteral distance (in degrees). The single-station magnitude is calculated from waveforms within a time window from the P onset (t_P) to $2(t_S - t_P)$, where t_S is the predicted S arrival based on a 1D Earth model. Because the high-frequency foreshock signal grows (Figure 4c), the single-station magnitude estimates increase with increasing distance, from M_L 1.89 for NEA2 to M_L 3.64 for KTH. The average M_L for all 15 stations is the event magnitude (3.0), which is the formally reported magnitude for the event.

(a) 2025 VLFE

(b) 2025 earthquake

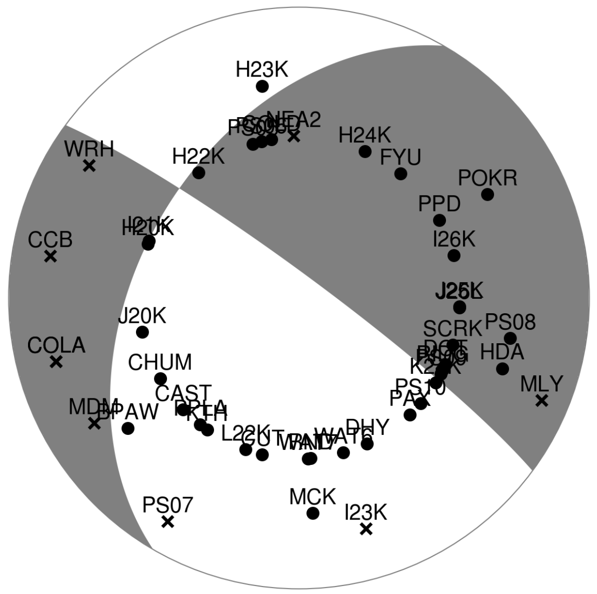

(c) 2019 earthquake

(d) 2022 earthquake

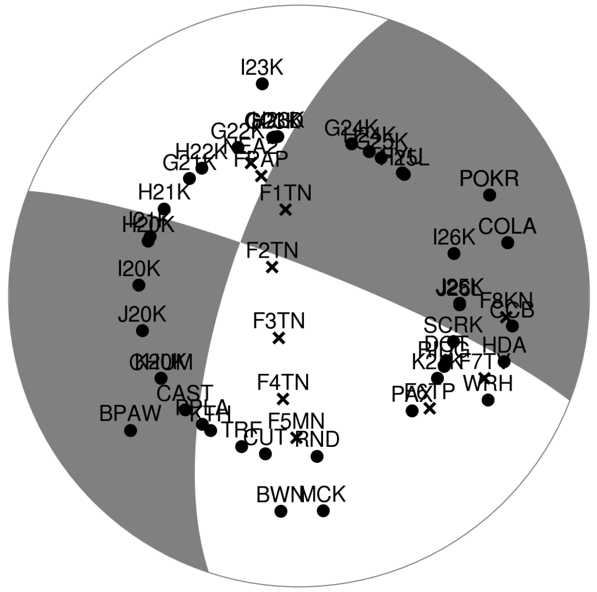

Figure S2: Station coverage for four events in our study. The stations are plotted at their ray-path piercing point on the lower-hemisphere of the beachball. Upward ray paths are depicted by the X symbols and plotted at their antipode. Downward ray paths are depicted by the circle symbols. (The radial coordinate of each symbol depends on the choice of 1D Earth model.) All stations are within 300 km of each epicenter.

(a) 2025 VLFE (b) 2025 earthquake

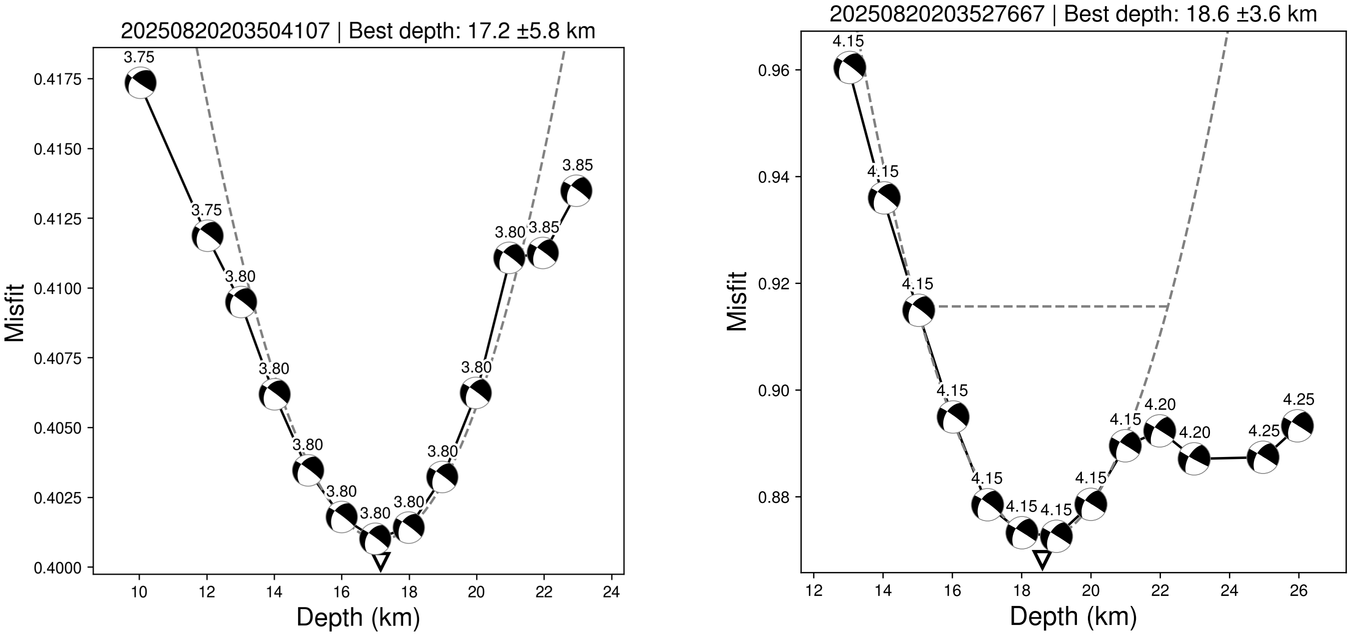

(c) 2019 earthquake (d) 2022 earthquake

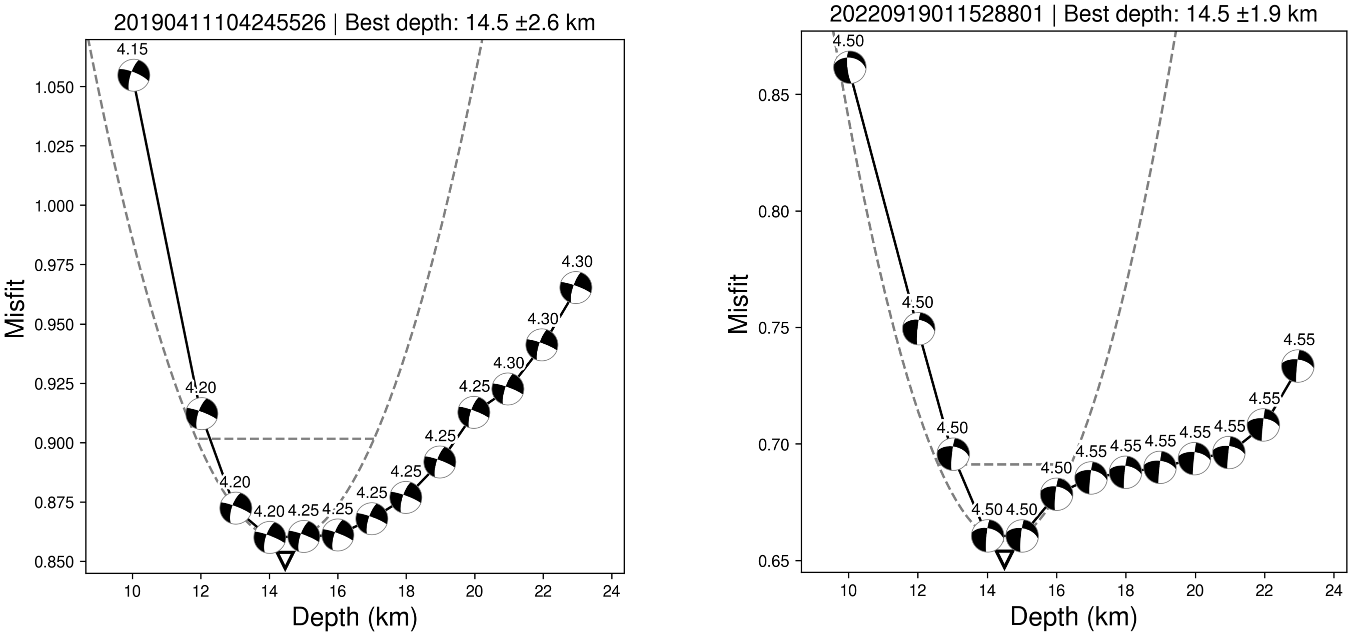

Figure S3: Depth grid searches for four events in our study (Tabs. 1 and S1). The depth search increment is 1 km, the magnitude increment is $\Delta M_{\mathrm{w}} = 0.05$. The white triangle marks the best-fitting depth, and the uncertainty is depicted by the horizontal line, which marks a misfit value 5% higher than the global minimum. Note that in (a), the horizontal line lies outside the limits of the plot.

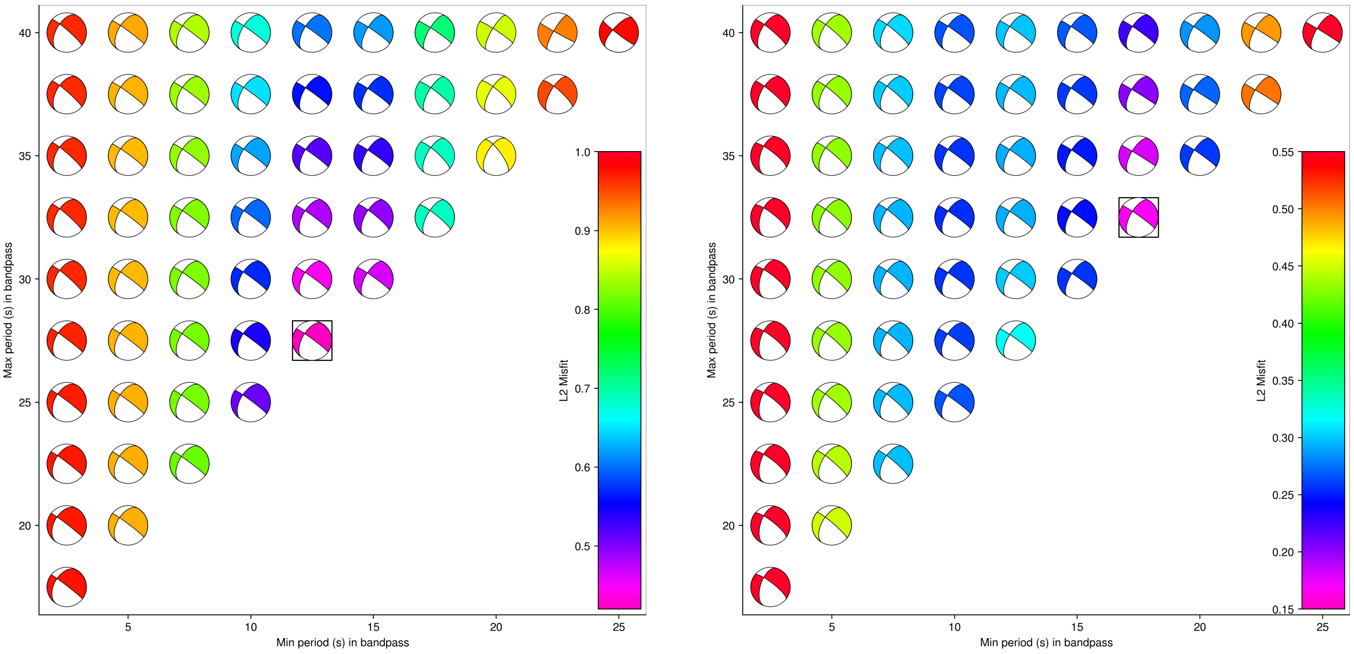

(a) 2025 VLFE

(b) 2025 earthquake

Figure S4: Variations in best-fitting moment tensors as a function of bandpass for the 2025 VLFE (a) and the 2025 earthquake (b). The x-axis is the minimum period of the bandpass, and the y-axis is the maximum period. In total, there are 55 different bandpasses. Each moment tensor beachball is colored by its misfit. The allowable time shifts are ±3 s. The beachball inside the black square is the overall lowest misfit solution among all the bandpasses. Our choice of 12.5–27.5 s is based on the VLFE results in (a).

Figure S5: The impact of adjusting the allowable time shifts for the 2025 events. The origin time is set to the AEC VLFE onset time of 20:34:45.2. The seismograms are filtered 12.5–27.5 s. (a) Allowable time shifts of ±30 s. The estimated source is for the first event, which is a VLFE. (b) Allowable time shifts of ±50 s. The estimated source is for the second event, which is an earthquake. These results are similar to those in Figure S6.

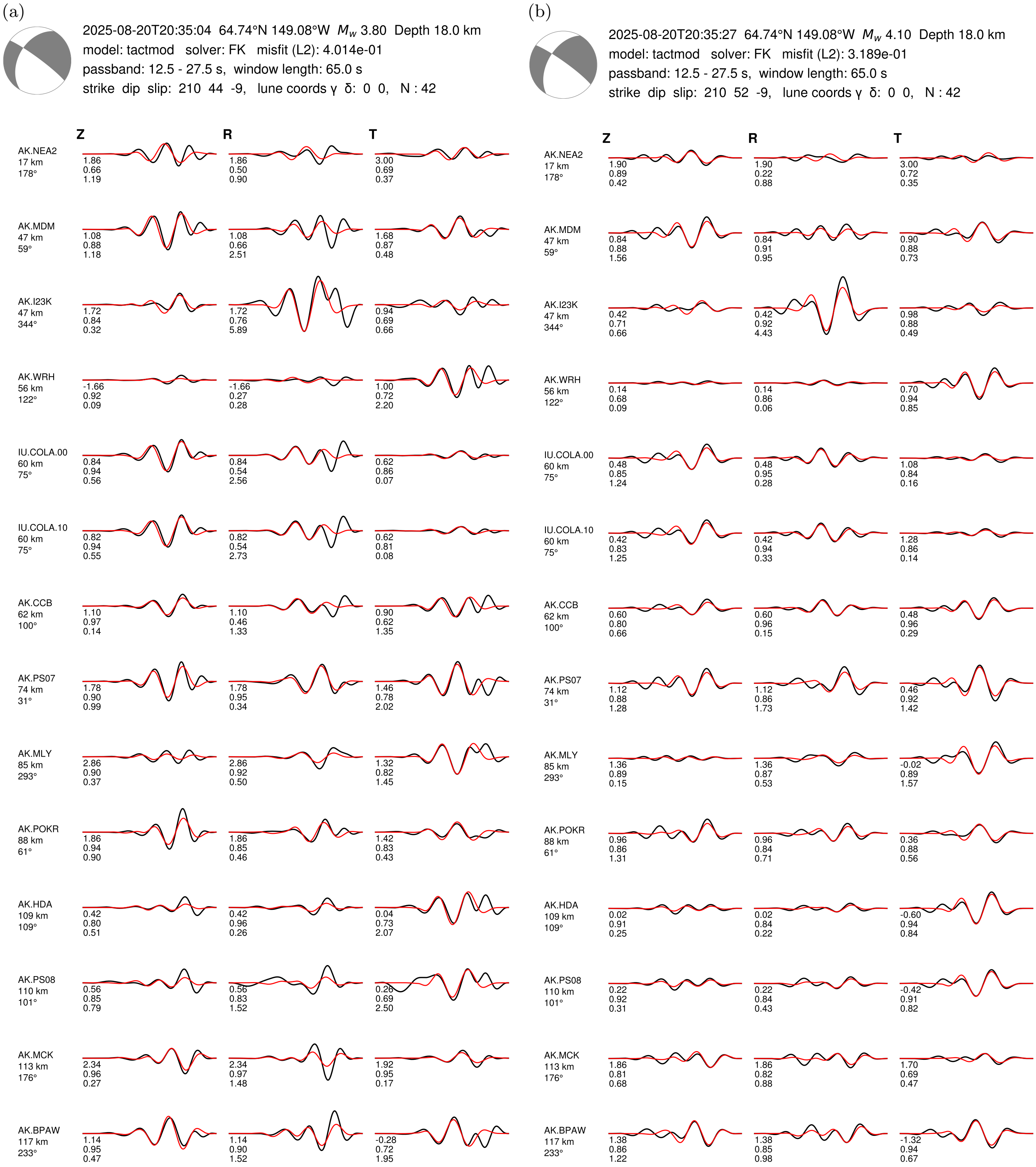

Figure S6: Same as Figure 2, but here the earthquake moment tensor estimation in (b) is set identically to (a), in terms of the chosen stations, time windows (65 s for Z, R, and T only), and bandpass (12.5–27.5 s). As a result, the estimated source parameters for the earthquake are slightly different (Table S1). See also Figure S5.

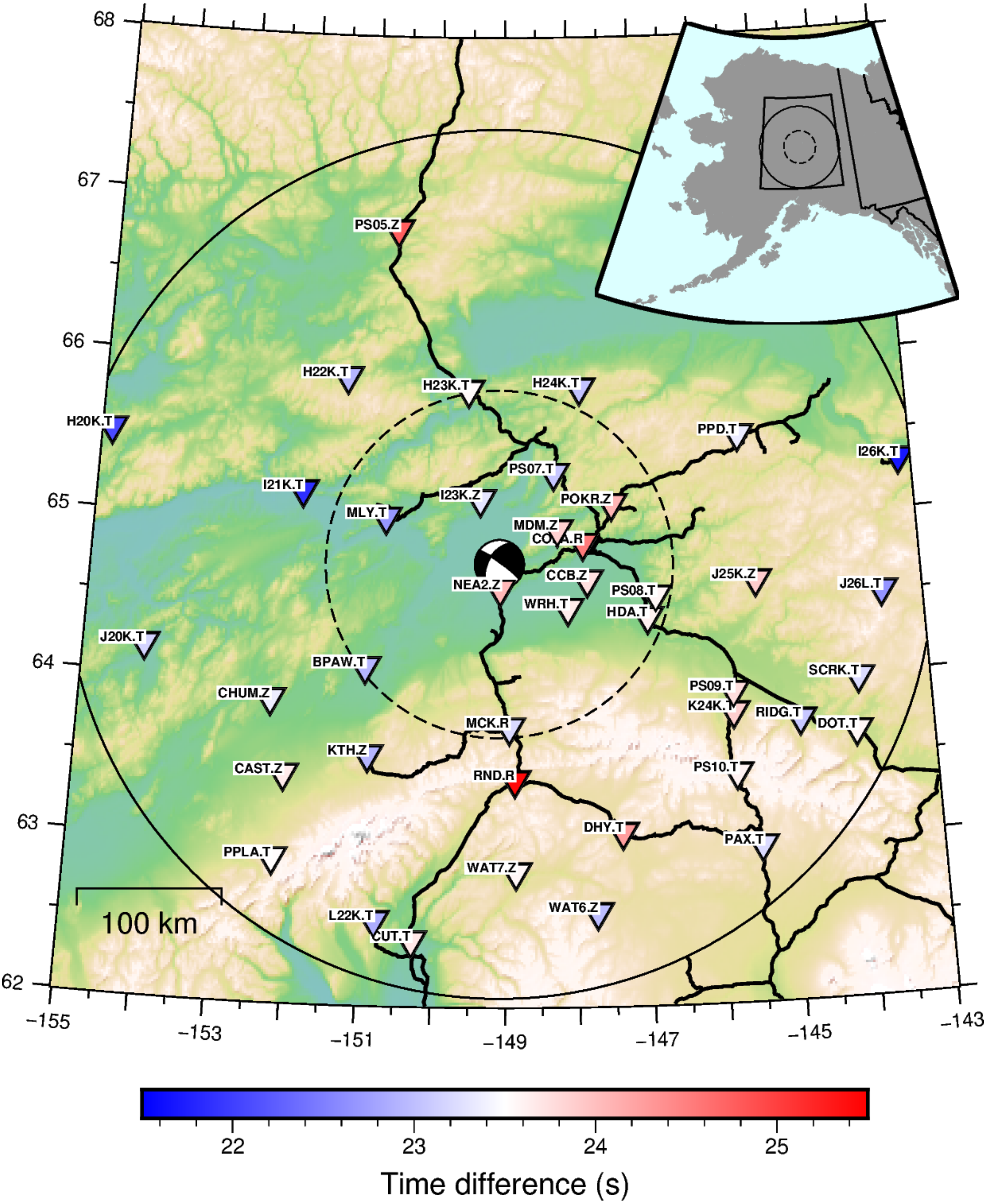

Figure S7: Time shifts between VLFE and earthquake waveforms derived from seismograms filtered 12.5–27.5 s, as shown in Figures S8–S12. The mean time shift value is 23.6 ± 0.5 s, which is based on the 13 stations within 120 km of the epicenter; this subset region is depicted by the dashed circle. The outer circle (300 km radius) encompasses all 41 stations used to estimate the 2025 VLFE (Figure 2a).

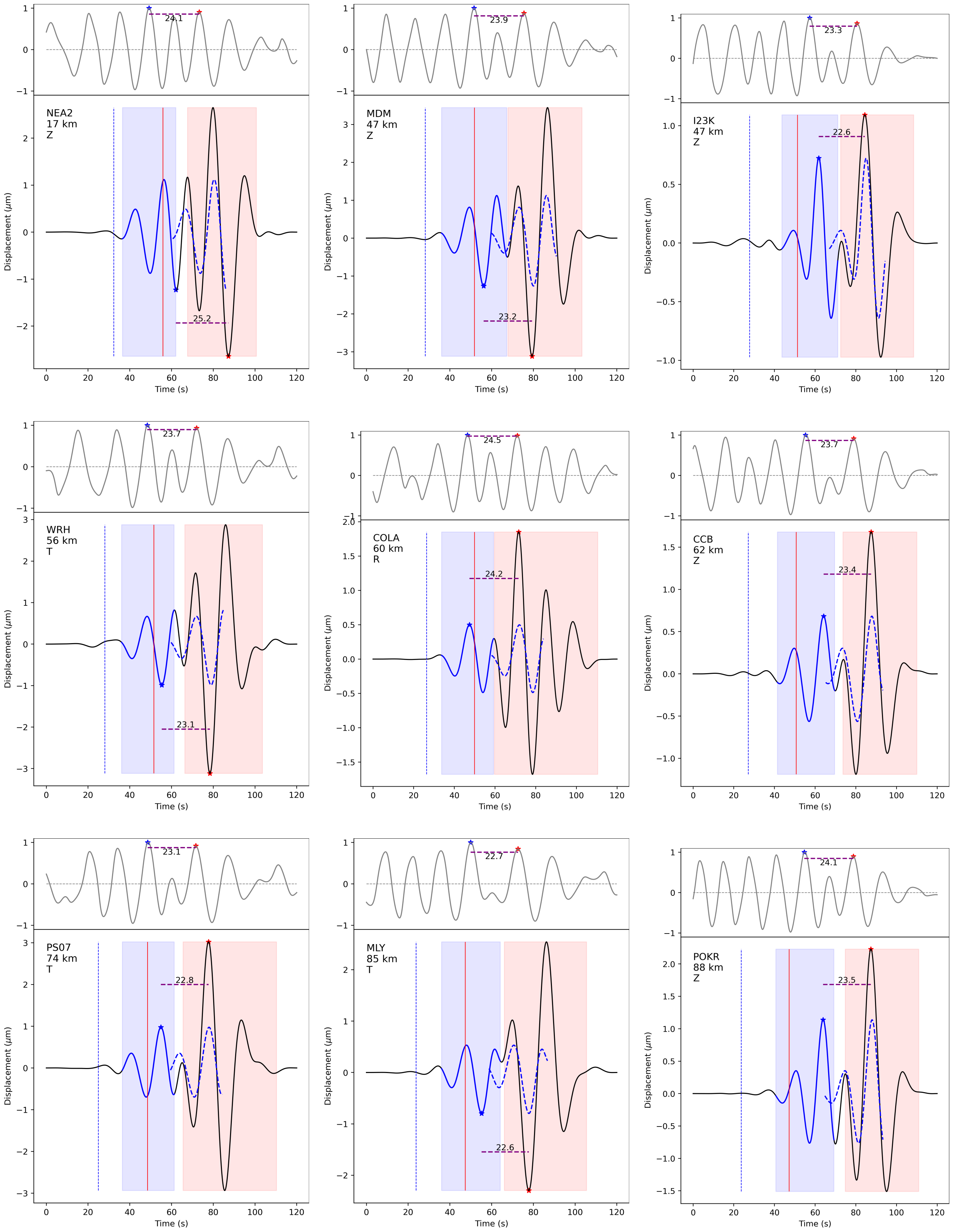

Figure S8: Figures S8–S12 shows the cross-correlation time shift measurements between the VLFE and earthquake waveforms for the 41 stations displayed in Figure S7. See main paper for details.

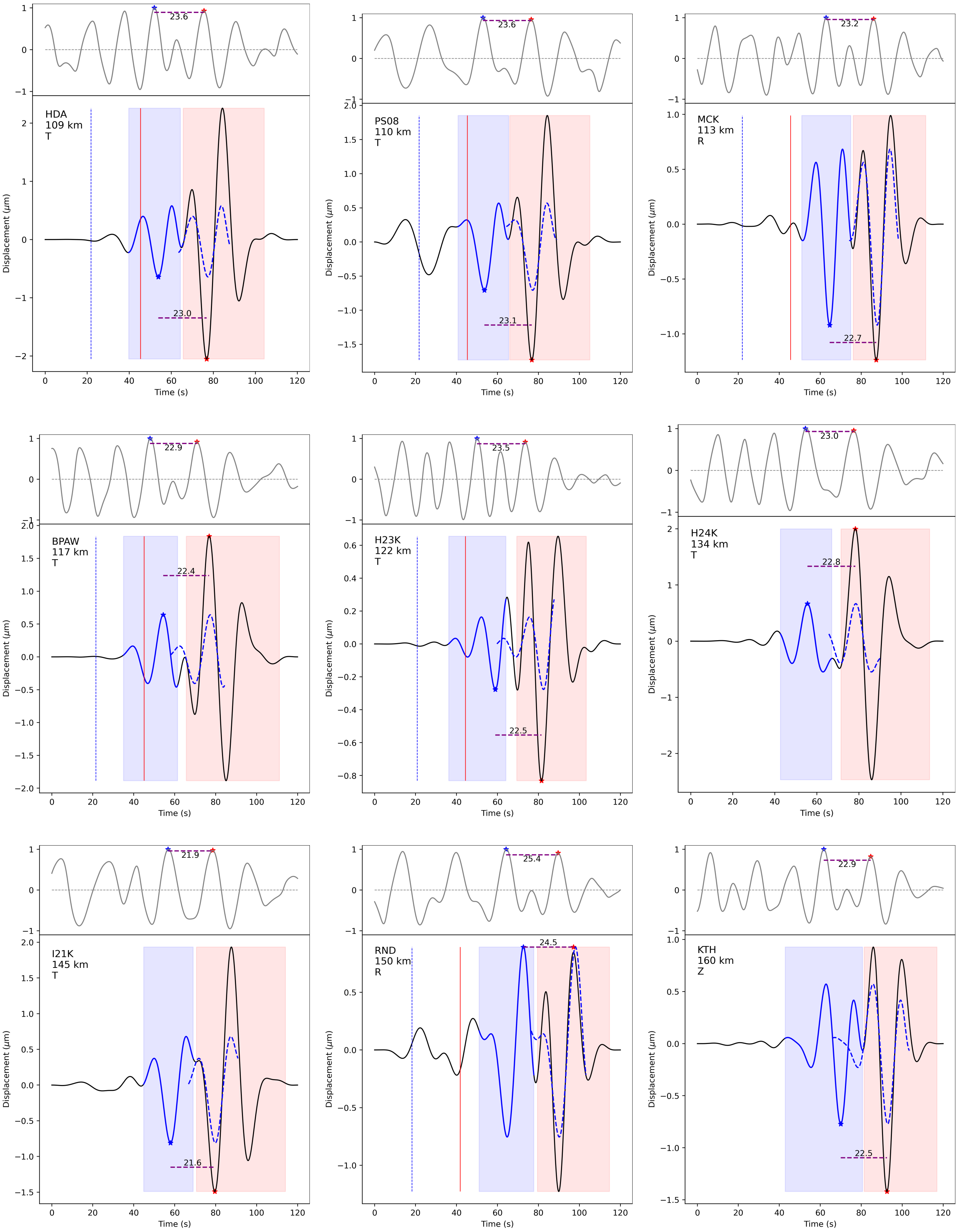

Figure S9: Figures S8–S12 shows the cross-correlation time shift measurements between the VLFE and earthquake waveforms for the 41 stations displayed in Figure S7. See main paper for details.

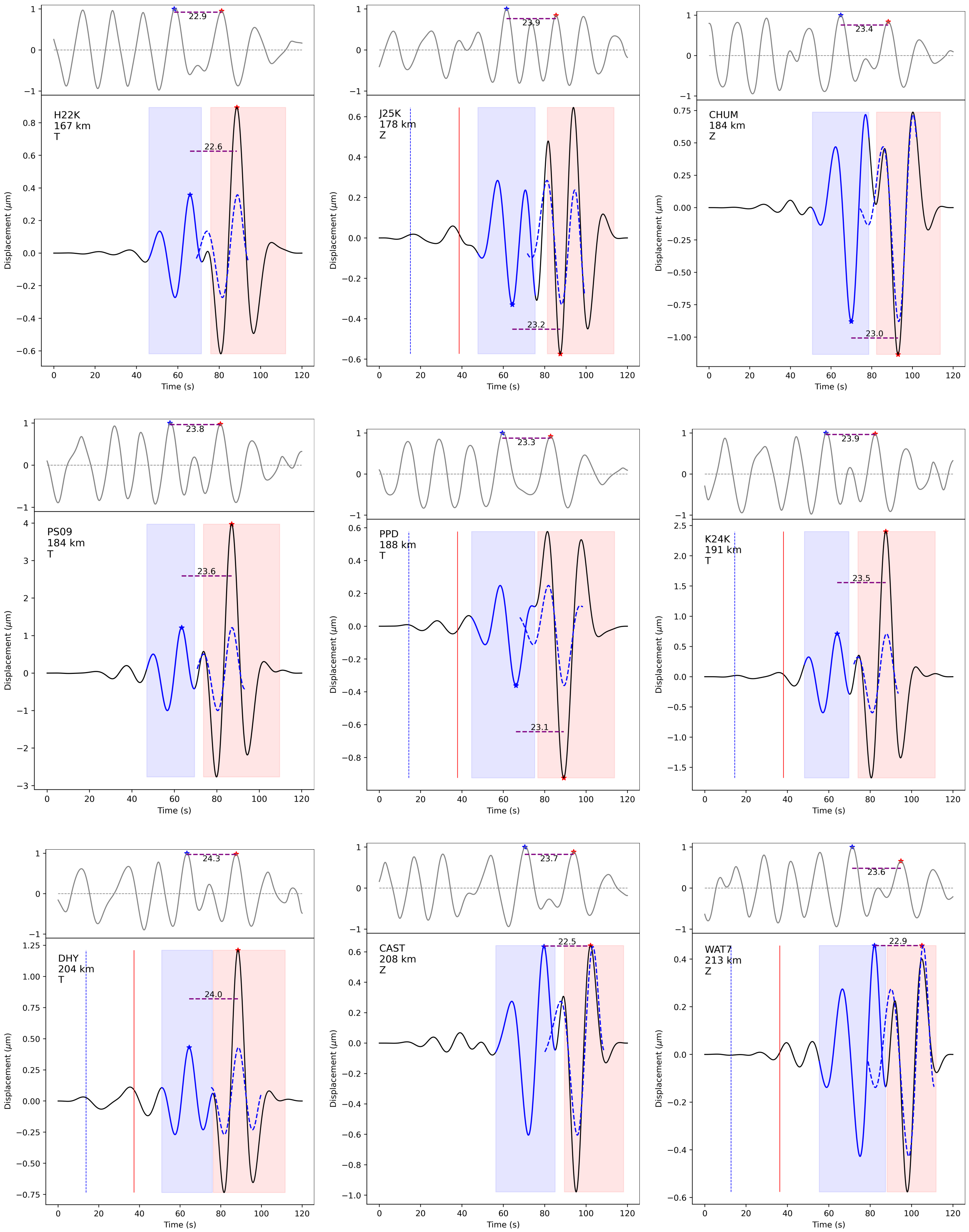

Figure S10: Figures S8–S12 shows the cross-correlation time shift measurements between the VLFE and earthquake waveforms for the 41 stations displayed in Figure S7. See main paper for details.

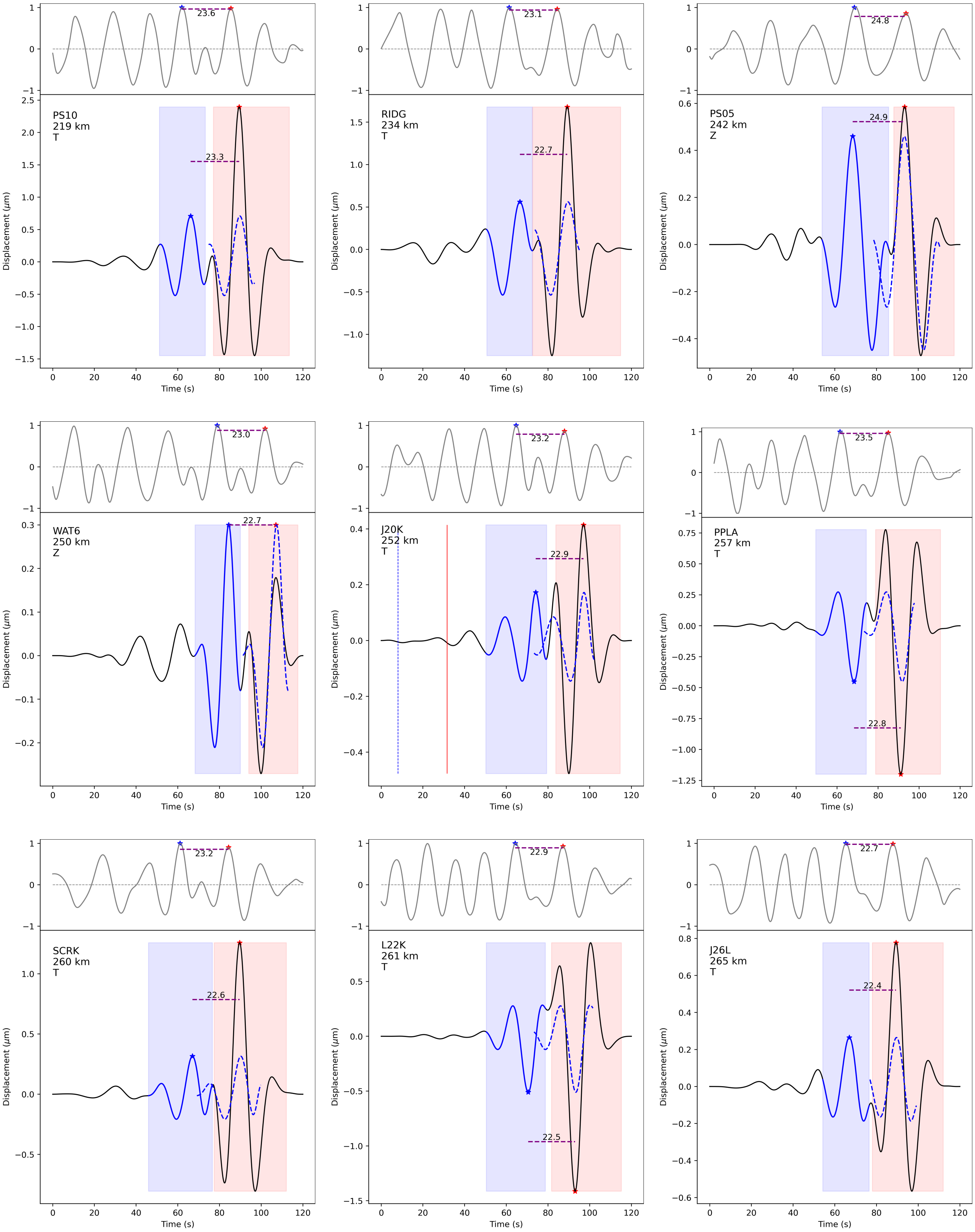

Figure S11: Figures S8–S12 shows the cross-correlation time shift measurements between the VLFE and earthquake waveforms for the 41 stations displayed in Figure S7. See main paper for details.

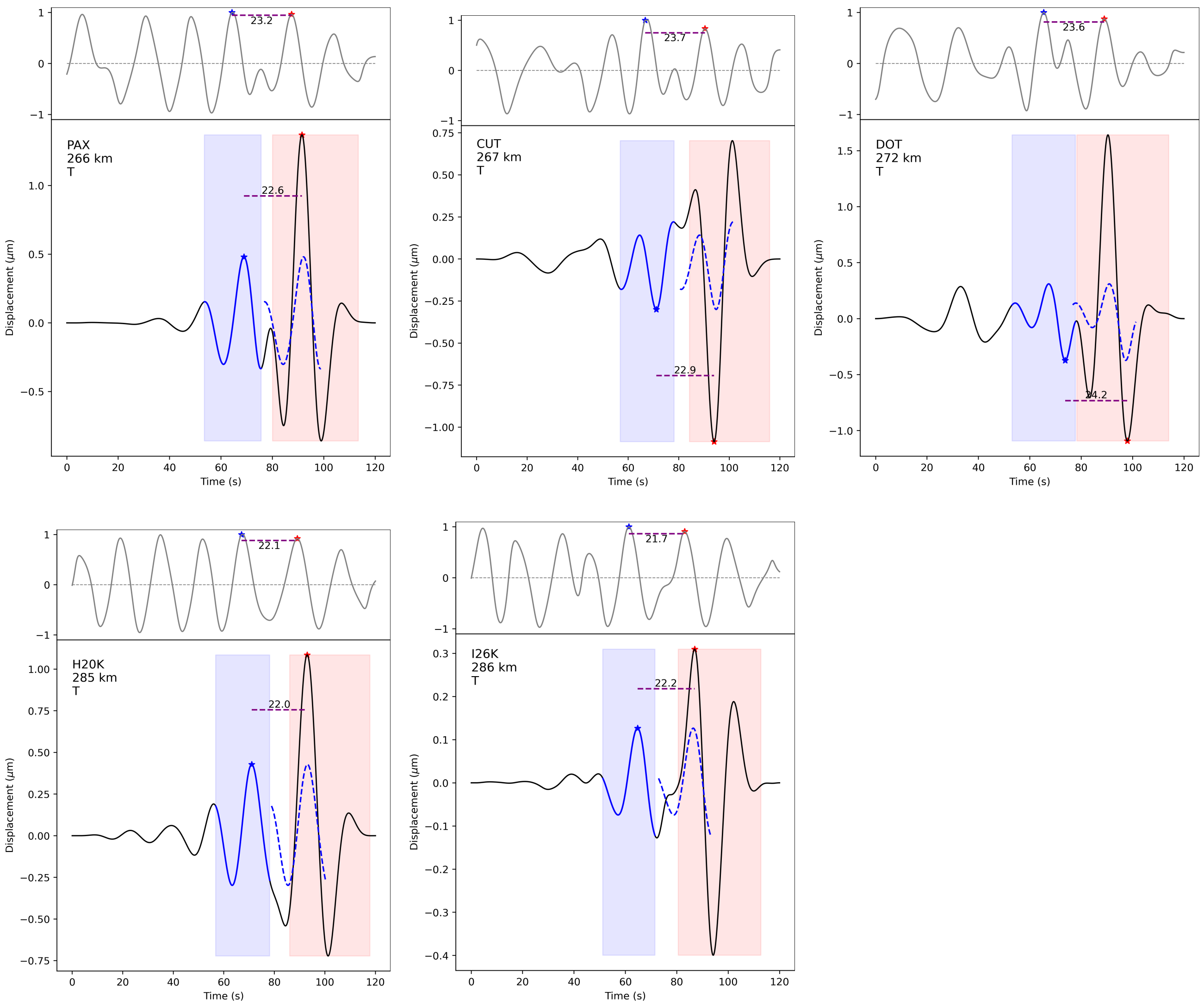

Figure S12: Figures S8–S12 shows the cross-correlation time shift measurements between the VLFE and earthquake waveforms for the 41 stations displayed in Figure S7. See main paper for details.

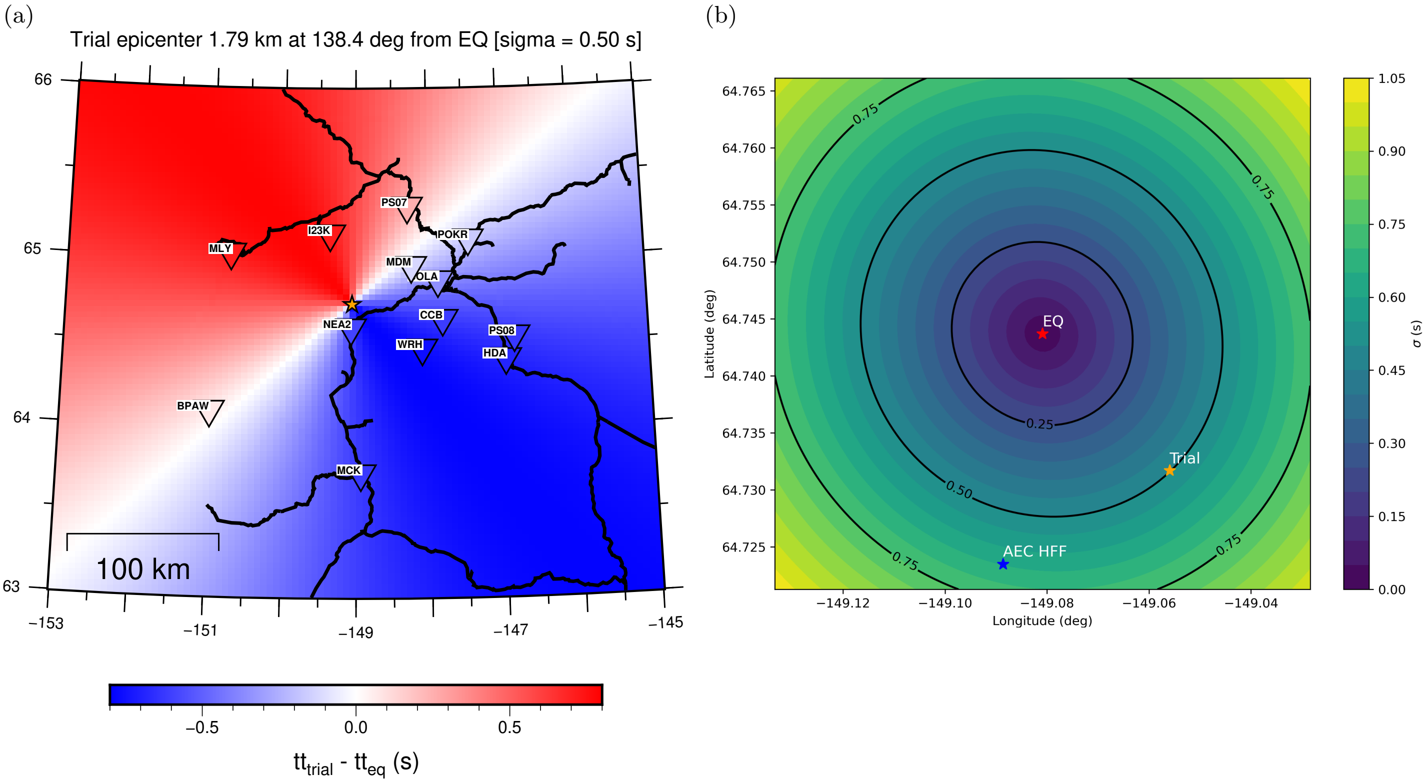

Figure S13: Grid search to examine the influence of a VLFE epicenter that is offset laterally from the 2025 earthquake epicenter. All calculations are based on theoretical travel times using straight-line ray paths. (a) Example grid of $tt^i(\mathbf{x}_{\mathrm{trial}}) - tt^i(\mathbf{x}_{\mathrm{eq}})$, where $tt^i(\mathbf{x}) = \|\mathbf{x}^i - \mathbf{x}\|/U$ is the traveltime from epicenter $\mathbf{x}$ to the ith station, and $U = 2.26$ km/s is the assumed group speed, which is based on the observed waveforms (Figures S8 and S9) for the closest 13 stations. The earthquake epicenter is $\mathbf{x}_{\mathrm{eq}}$. The trial epicenter $\mathbf{x}_{\mathrm{trial}}$—representing the VLFE—is 1.8 km southeast of the earthquake epicenter. Because this trial epicenter is southeast of the earthquake epicenter, the traveltimes to northwest stations are longer, and therefore the differential times are positive (red). For this trial epicenter, the resulting standard deviation in the 13 differential times is $\sigma(\mathbf{x}_{\mathrm{trial}}) = \mathrm{std}[tt^i(\mathbf{x}_{\mathrm{trial}}) - tt^i(\mathbf{x}_{\mathrm{eq}})] = 0.50$ s, represented by the color value (greenish) at the location of the orange star in (b). (b) A 5 km × 5 km uniform grid of $\sigma(\mathbf{x}_{\mathrm{trial}})$ for candidate VLFE epicenters $\mathbf{x}_{\mathrm{trial}}$. The grid is exactly centered on $\mathbf{x}_{\mathrm{eq}}$, which helps to convey the slight differences in azimuth due to the irregular coverage of the 13 stations. The three colored stars are the AEC earthquake epicenter ("EQ": red), the AEC HFF epicenter ("AEC HFF": blue), and a trial epicenter ("Trial": orange) corresponding to (a).

(a) 2019 M_w 4.2 earthquake

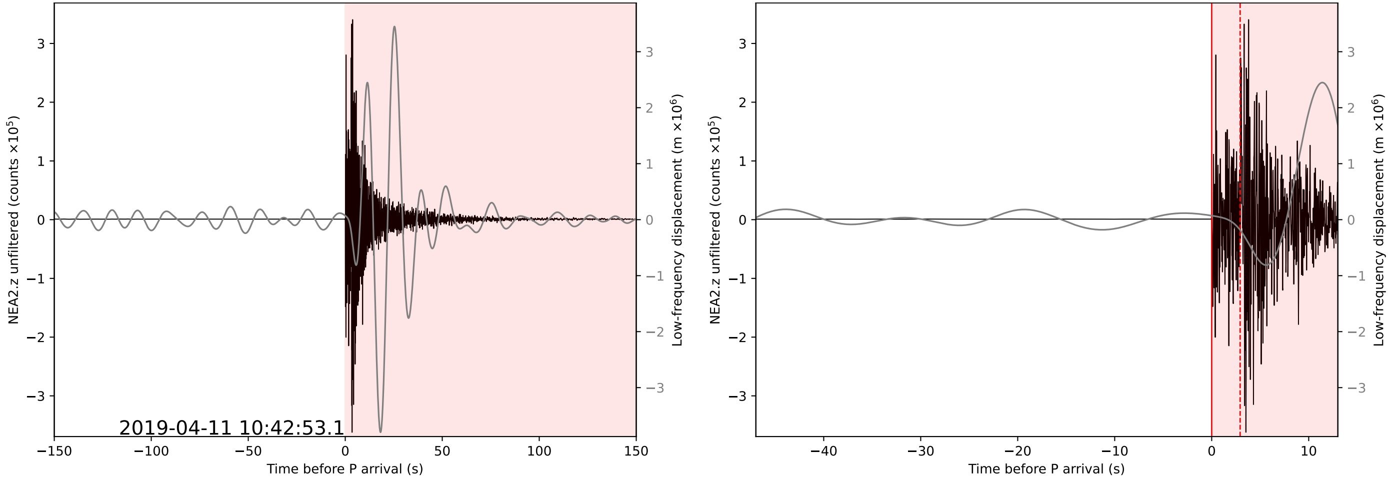

(b) 2022 M_w 4.5 earthquake

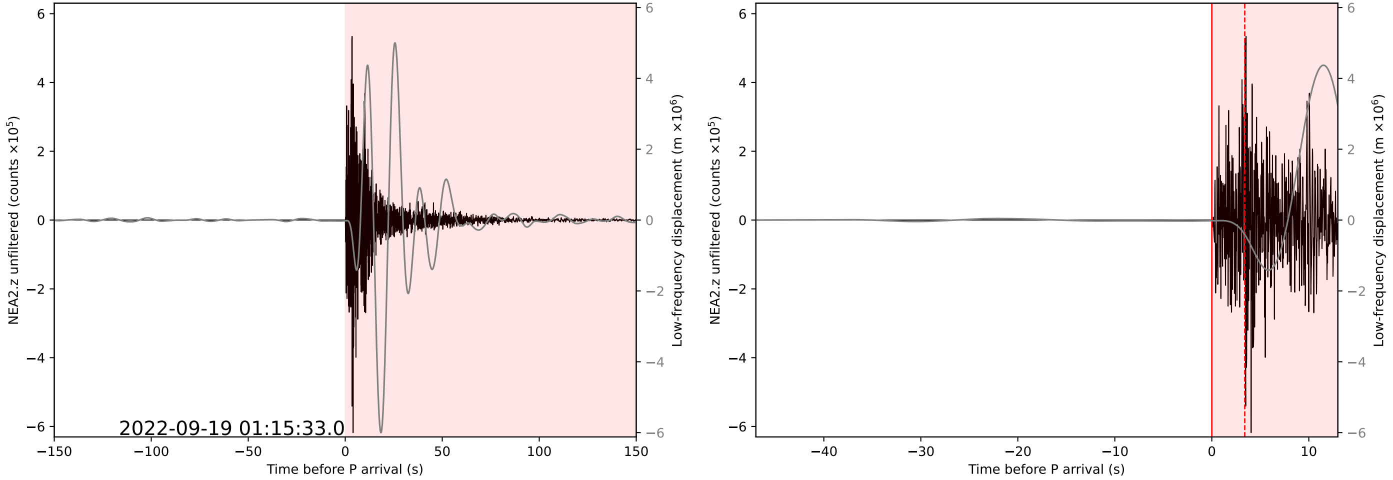

(c) 2025 M_w 4.2 earthquake and VLFE

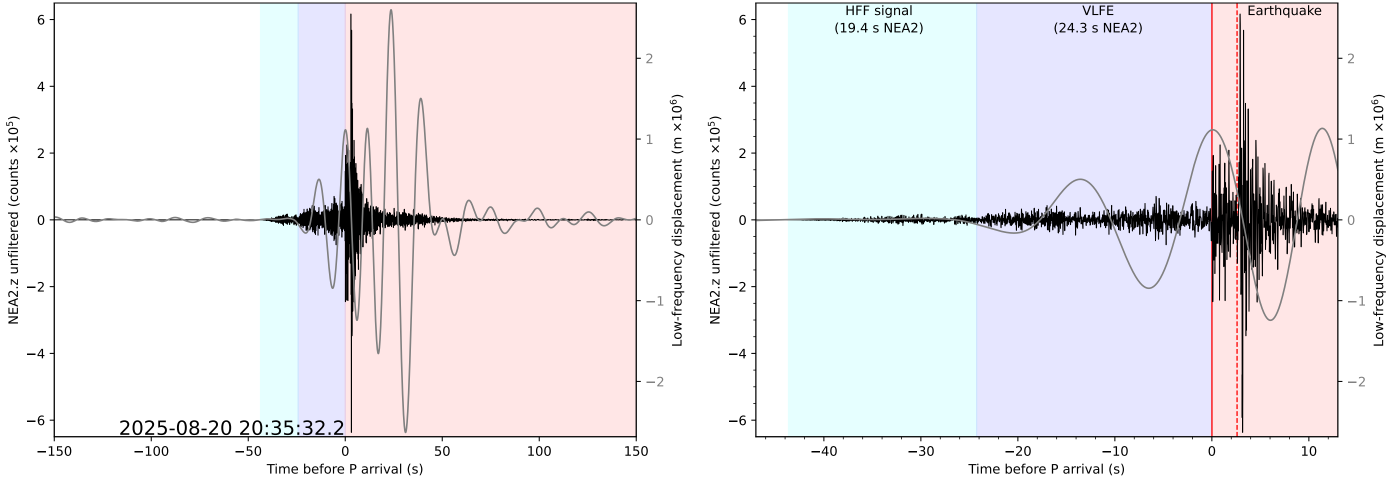

Figure S14: Seismograms recorded at station NEA2 for three events. Each plot shows two vertical-component seismograms; one is unfiltered (black), the other is causally (one-pass) bandpass-filtered between periods 12.5–27.5 s (gray). (a)-(left) 2019 M_w 4.2 earthquake. The time axis is centered and referenced to the P arrival time ($t = 0$), which is labeled at the bottom of the plot. (a)-(right) Same as left, but displaying a 60-s time window. (b) 2022 M_w 4.5 earthquake. (c) 2025 M_w 4.2 earthquake and VLFE. Three of these plots appear in Figure 4.

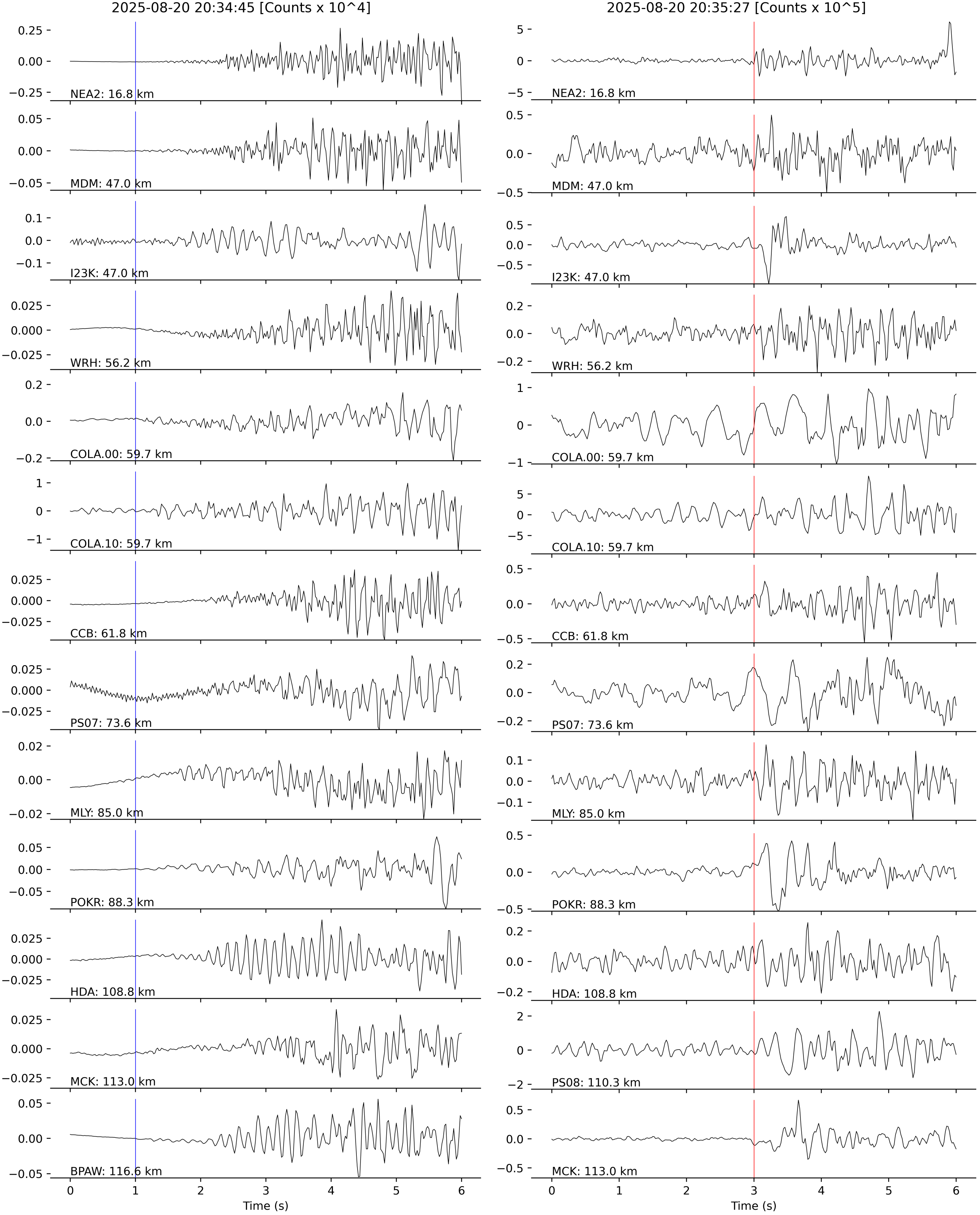

(a) 2025 VLFE

(b) 2025 earthquake

Figure S15: Unfiltered record sections for the vertical component for the closest 12 stations to the 2025 VLFE+earthquake. Seismograms are sorted by increasing epicentral distance from top to bottom. (a) 2025 $M_\mathrm{w}\,3.8$ VLFE. $t = 1$ (blue line) marks the catalog onset time for this event. (b) 2025 $M_\mathrm{w}\,4.2$ earthquake. $t = 3$ (red line) marks the P onset time. The pre-P signals are not noise; they are from the preceding VLFE.

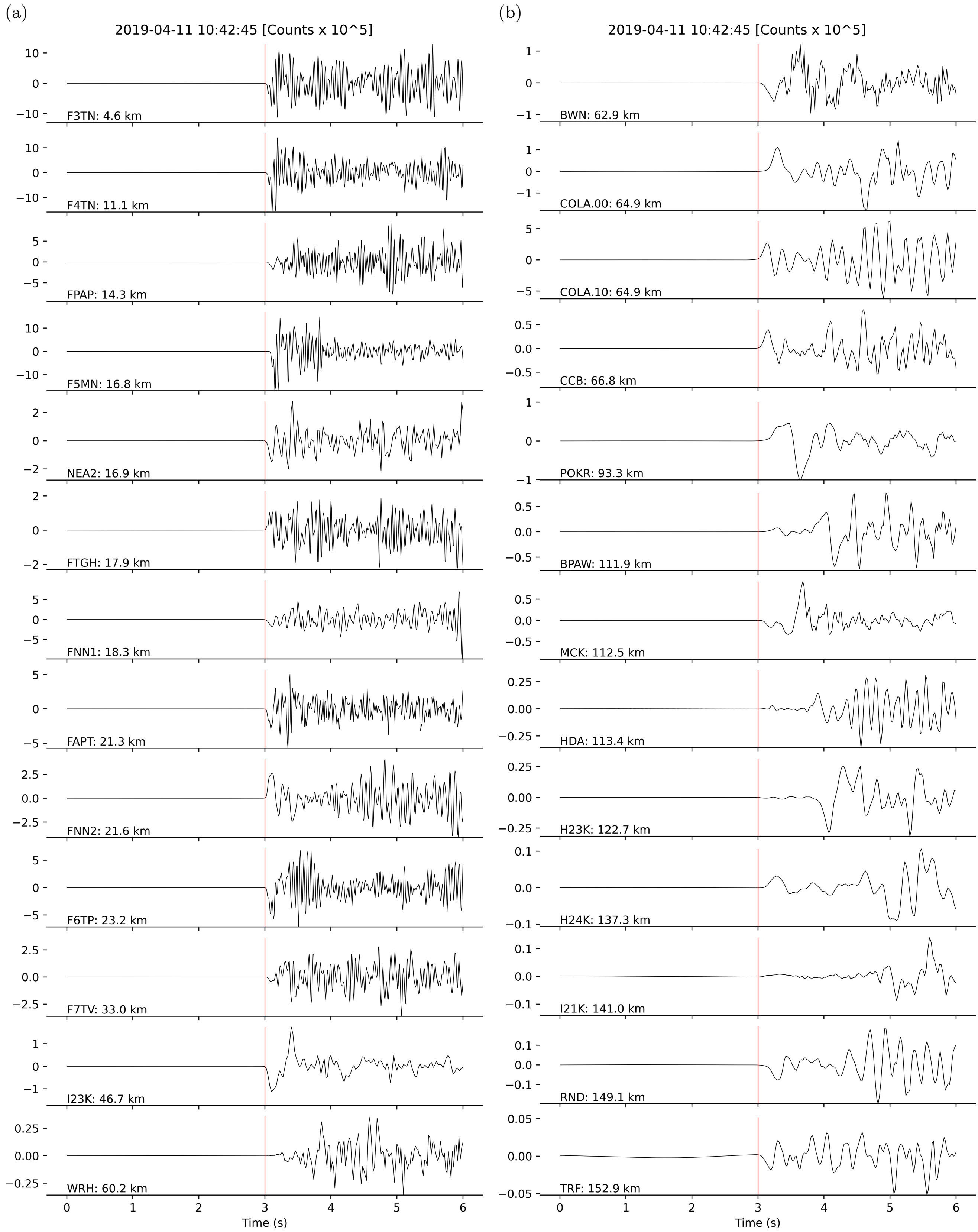

Figure S16: Unfiltered record sections for the vertical component for the 2019 M_w 4.2 earthquake. Seismograms are sorted by increasing epicentral distance, with the distance labeled next to the station name. $t = 3$ (red line) marks the P onset time. Note the lack of pre-P signal, in comparison with the 2025 M_w 4.2 earthquake in Figure S15b.

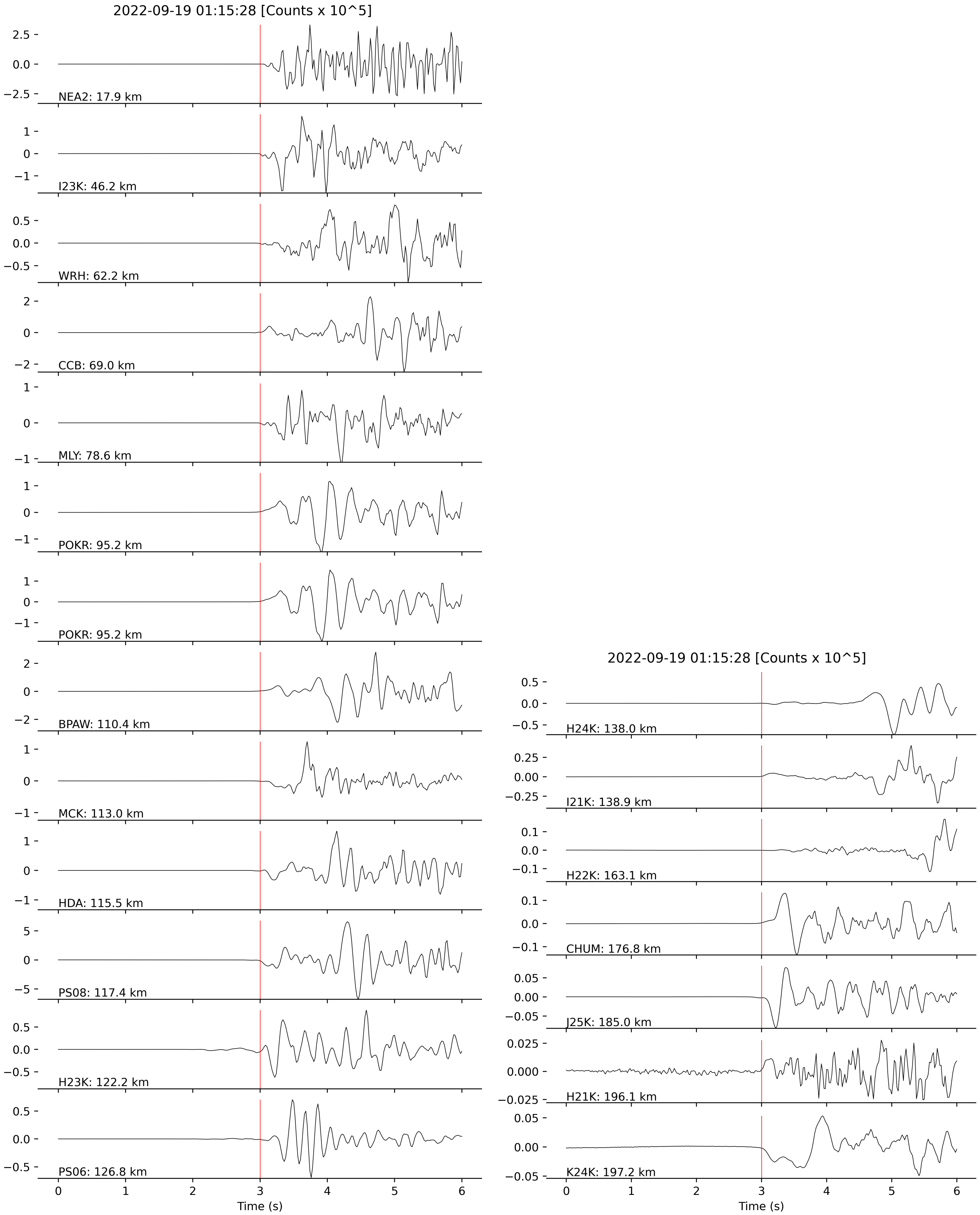

Figure S17: Unfiltered record sections for the vertical component for the 2022 M_w 4.5 earthquake. Seismograms are sorted by increasing epicentral distance, with the distance labeled next to the station name. $t = 3$ (red line) marks the P onset time. Note the lack of pre-P signal, in comparison with the 2025 M_w 4.2 earthquake in Figure S15b.

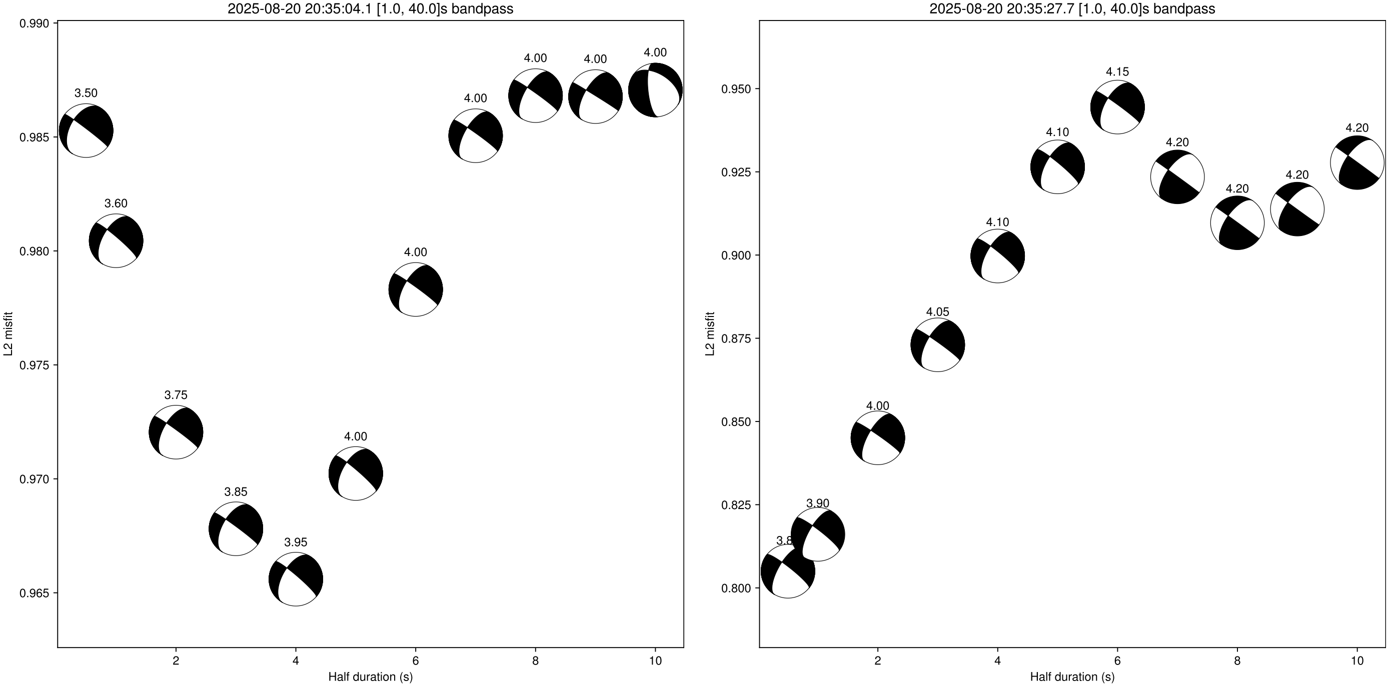
(a) 2025 VLFE

(b) 2025 earthquake

Figure S18: Estimating the source duration for the 2025 VLFE (a) and earthquake (b) using the bandpass of 1–40 s and three full-length time windows for vertical, radial, and transverse components. For each event, we estimate double-couple moment tensors using 11 different source half-durations ranging from 0.5 s to 10.0 s. The magnitude and orientation of each moment tensor are allowed to vary. The source time function used is a trapezoid with unit area, symmetric around $t = 0$, where the base of the trapezoid is defined by $2\tau_\mathrm{h}$, where τ_h is the half-duration, and the top of the trapezoid is defined by $2(\tau_\mathrm{h} - \tau_\mathrm{r})$, where τ_r is the rise time. (a) 2025 VLFE. The best-fitting half-duration is 4.0 s. (b) 2025 earthquake. The best-fitting half-duration is 0.5 s (or lower).

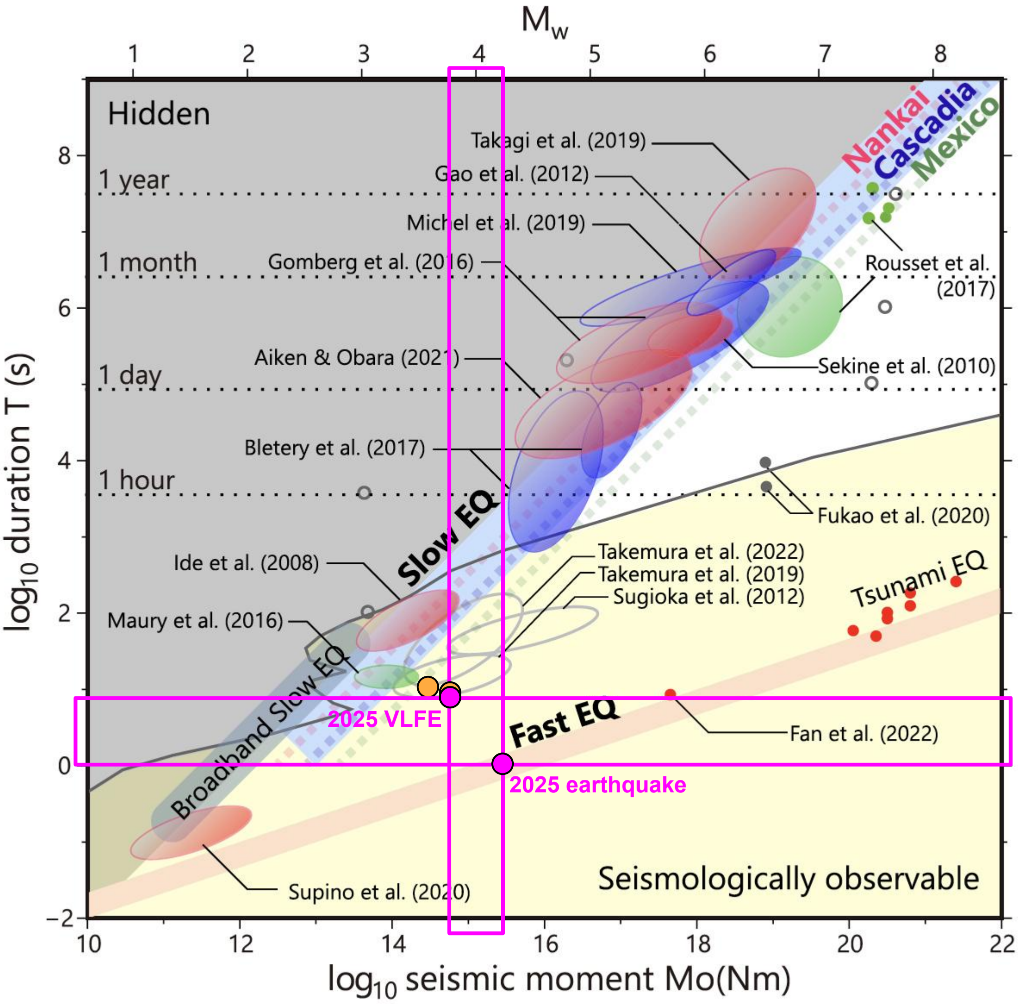

Figure S19: Annotated version of Figure 3 of Ide and Beroza (2023), with the two magenta circles depicting the durations and magnitudes of the 2025 VLFE (8.0 s, M_w 3.80) and the 2025 earthquake (1.0 s, M_w 4.15). The durations are from Figure S18, and the preferred magnitudes are from Figure 2. Also plotted are two orange circles for the 2013 and 2015 VLFEs reported in Tape et al. (2018). The three VLFEs (2013, 2015, 2025) are close to the ellipse representing the events of Takemura et al. (2019).